J. Fluid Mech. (2002), *vol.* 457, *pp.* 35–78. © 2002 Cambridge University Press
DOI: 10.1017/S0022112001007443 Printed in the United Kingdom

Statistical geometry of subgrid-scale stresses determined from holographic particle image velocimetry measurements

By BO TAO[1]†, JOSEPH KATZ[1,2] AND CHARLES MENEVEAU[1,2]

[1]Department of Mechanical Engineering,

[2]Center for Environmental and Applied Fluid Mechanics,
The Johns Hopkins University Baltimore, MD 21218, USA

(Received 21 September 2000 and in revised form 25 July 2001)

Three-dimensional velocity distributions of a turbulent flow in the core region of a square duct at $Re_H = 1.2 \times 10^5$ are measured using holographic particle image velocimetry (HPIV). Spatial filtering of the $136 \times 130 \times 128$ velocity vector maps enables calculation of subgrid-scale (SGS) stresses and parameters based on the filtered velocity gradients, such as the filtered strain-rate tensor and vorticity vector. Probability density functions (p.d.f.) of scalar parameters characterizing eigenvalue structures confirm that the most probable strain-rate topology is axisymmetric extension, and show that the most probable SGS stress state is axisymmetric contraction. Conditional sampling shows that high positive SGS dissipation occurs preferentially in regions with these preferred strain-rate and stress topologies. High negative SGS dissipation (backscatter) occurs preferentially in regions of axisymmetric contracting SGS stress topology, but is not associated with any particular strain-rate topology. The nonlinear model produces the same trends but tends to overpredict the likelihood of the preferred stress state.

Joint p.d.f.s of relative angles are used to investigate the alignments of the SGS stress eigenvectors relative to the vorticity and eigenvectors associated with eddy viscosity and similarity/nonlinear models. The results show that the most extensive SGS stress eigenvector is preferentially aligned at 32° to the most contracting strain-rate eigenvector. This alignment trend persists, with some variations in angle and peak probability, during conditional samplings based on the SGS dissipation rate, vorticity and strain-rate magnitudes. The relative alignment of the other two stress and strain-rate eigenvectors has a bimodal behaviour with the most contracting and intermediate stress eigenvectors 'switching places': from being aligned at 32° to the most extensive strain-rate eigenvector to being parallel to the intermediate strain-rate eigenvector. Conditional sampling shows that one of the alignment configurations occurs preferentially in regions of high vorticity magnitude, whereas the other one dominates in regions where the filtered strain-rate tensor has axisymmetric contracting topology. Analysis of DNS data for isotropic turbulence at lower *Re* shows similar trends.

Conversely, the measured stress eigenvectors are preferentially aligned with those of the nonlinear model. This alignment persists in various regions of the flow (high vorticity, specific flow topologies, etc). Furthermore, the alignment between the strain-rate and nonlinear model tensors also exhibits a bimodal behaviour, but the alignment angle of both configurations is 42°. Implications of alignment trends on SGS dissipation are explored and conditions for high backscatter are identified based on the

† Present address: School of Civil Engineering, Purdue University, West Lafayette, IN 47907, USA.

orientation of the stress eigenvectors. Several dynamical and kinematical arguments are presented that may explain some of the observed preferred alignments among tensors. These arguments motivate further analysis of the mixed model, which shows good alignment properties owing to the dominance of the Leonard stress on the alignments. Nevertheless, the data also show that the mixed model produces some unrealistic features in probability distributions of SGS dissipation, and unphysical eigenvector alignments in selected subregions of the flow.

1. Introduction

Turbulence inherently spans a wide range of length scales, from the large, energy containing ones down to small, viscous dissipation scales. Turbulence is also inherently three-dimensional. The goal of the present work is to characterize important features of the three-dimensional structure of interactions among different scales in turbulence, using holographic particle image velocimetry (HPIV). The interactions between large and small scales are of particular relevance to large eddy simulation (LES). For recent reviews of LES, see e.g. Lesieur & Métais (1996), Piomelli (1999), and Meneveau & Katz (2000). In LES, the small scales are represented by the SGS stress tensor τ_{ij}, defined as

$$\tau_{ij} = \widetilde{u_i u_j} - \tilde{u}_i \tilde{u}_j, \tag{1.1}$$

where the tilde denotes spatial filtering at scale Δ. The stress tensor τ_{ij} must be modelled in terms of the resolved variables. The model may involve, among others, parameters of the large-scale velocity gradient tensor such as the filtered vorticity vector ($\tilde{\omega}_i$) and the filtered strain-rate tensor ($\tilde{S}_{ij}$), defined as, respectively:

$$\tilde{\omega}_i = \varepsilon_{ijk} \partial \tilde{u}_k / \partial x_j, \tag{1.2}$$

$$\tilde{S}_{ij} = \tfrac{1}{2}(\partial \tilde{u}_i / \partial x_j + \partial \tilde{u}_j / \partial x_i). \tag{1.3}$$

Direct numerical simulation (DNS) has provided valuable information about turbulent flow phenomena, and played an important role in the development of improved turbulence models (see e.g. Moin & Mahesh 1998). A limitation of DNS is that all scales of the flow must be properly resolved and as a result, it is limited to low Reynolds numbers, at least for the foreseeable future. Consequently, experimental data are essential if flows at high Reynolds numbers are to be used for development of physics-based models.

1.1. *Background on PIV-based experimental studies of some simple subgrid-scale models*

In recent years, we have studied fundamental properties of subgrid-scale (SGS) stresses and tested models using two-dimensional PIV data (Liu, Meneveau & Katz 1994, 1995; Liu, Katz & Meneveau 1999; Meneveau & Katz 1999*a*). These analyses have provided considerable insight into the dynamics of SGS stresses in isotropic and rapidly strained turbulence. Planar PIV data were also used in Bastiaans, Rindt & van Steenhoven (1998) for SGS analysis of a plume. However, two-dimensional PIV measurements inherently provide only partial data (e.g. only three of the six tensor components) on the stress and filtered strain-rate distributions. In several instances during these studies it has become evident that understanding the relationships between filtered vorticity, strain-rate and stress tensors requires three-dimensional data on the flow structure. Consequently, we have developed and implemented a

holographic PIV system (Zhang, Tao & Katz 1997; Tao, Katz & Meneveau 1999*a*) to measure the three-dimensional velocity distributions over a finite volume at a high spatial resolution. Such data enables us to systematically examine the structural characteristics and alignment of the SGS stress and strain-rate tensors, the vorticity distribution, SGS dissipation and other related parameters.

On employing *a priori* testing (Piomelli, Moin & Ferziger 1988), it has been repeatedly observed that the Smagorinsky model,

$$\tau_{ij}^{s} = -2(c_s\Delta)^2|\tilde{\boldsymbol{S}}|\tilde{S}_{ij}, \tag{1.4}$$

exhibits very little correlation with the real stress, τ_{ij} (see e.g. Liu *et al.* 1994), resulting in a low correlation coefficient, $\rho(\tau_{ij}^{s}, \tau_{ij})$. In contrast, the scale similarity model

$$\tau_{ij}^{sim} = C_{sim}(\overline{\tilde{u}_i\tilde{u}_j} - \overline{\tilde{u}}_i\,\overline{\tilde{u}}_j), \tag{1.5}$$

where the overbar denotes a second filtering at a scale $\Delta' \geqslant \Delta$, and the nonlinear model

$$\tau_{ij}^{nl} = C_{nl}\Delta^2(\partial\tilde{u}_i/\partial x_k)(\partial\tilde{u}_j/\partial x_k), \tag{1.6}$$

perform significantly better in predicting the SGS stresses (Leonard 1974; Bardina, Ferziger & Reynolds 1980; Liu *et al.* 1994; Borue & Orszag 1998).

The rate at which kinetic energy is transferred from the resolved to the subgrid motions is described by the SGS dissipation $\Pi(\boldsymbol{x}, t) = -\tau_{ij}\tilde{S}_{ij}$ (Piomelli *et al.* 1991). To provide adequate SGS dissipation and to ensure stability for application of the similarity or nonlinear model in LES, Bardina *et al.* (1980) and Liu *et al.* (1994) propose a mixed model consisting of a similarity or nonlinear term and an eddy viscosity term:

$$\tau_{ij}^{mix} = C_{nl}\Delta^2(\partial\tilde{u}_i/\partial x_k)(\partial\tilde{u}_j/\partial x_k) - 2(c_s\Delta)^2|\tilde{\boldsymbol{S}}|\tilde{S}_{ij}. \tag{1.7}$$

With proper coefficients to match the mean dissipation, this model has been shown to perform well in a variety of flow configurations (see e.g. Meneveau & Katz 2000 for an overview of the growing number of applications). However, model coefficients based on the energy dissipation fail to predict the correct magnitude of the stresses. Furthermore, use of correlation coefficients to examine the SGS models does not provide complete information about tensor geometrical relationships, nor does it account for potential large differences in magnitudes between the real and modelled stresses. Therefore, in order to improve our understanding of the relationships between the subgrid and resolved scales, in this paper we will focus instead on the structural and alignment properties of the SGS stress tensor. Employing recently obtained holographic PIV measurements (Tao, Katz & Meneveau 2000), we compute the SGS stress tensors and parameters involving the filtered velocity gradient tensor, such as the vorticity and the strain-rate. We then examine the eigenvalue structures and eigenvector alignments of these tensorial parameters relative to each other using a geometrically invariant analysis. The results provide insight into some of the significant structural and alignment features of SGS stresses and provide a basis for further SGS model improvement.

1.2. *Background on statistical geometry of tensors and vectors in turbulence*

The three-dimensional alignments between vectors and tensor eigenvectors are important characteristics and manifestations of the dynamics of turbulent flows. They have been the focus of several recent studies. For instance, considerable attention has been given to determining the geometrical relationship between the vorticity vector and the

eigenvectors of the strain-rate tensor. DNS of isotropic and shear turbulence (Ashurst *et al.* 1987; Vincent & Meneguzzi 1994, etc.), and hot-wire measurements of grid-generated turbulence (Tsinober, Kit & Dracos 1992), have shown that the vorticity vector is preferentially aligned with the eigenvector corresponding to the intermediate eigenvalue of the strain-rate tensor, especially in strongly dissipative regions.

Other important parameters include the relative magnitudes of eigenvalues of tensors, giving information about the relative importance of particular eigenvectors. While examining the probability of strain states using DNS data, Lund & Rogers (1994) propose the following strain state parameter to characterize the deformation of a fluid element:

$$s^* = -3\sqrt{6}\alpha_s\beta_s\gamma_s/(\alpha_s^2 + \beta_s^2 + \gamma_s^2)^{3/2}, \tag{1.8}$$

where α_s, β_s and γ_s are the eigenvalues of the strain-rate tensor, ordered such that $\alpha_s \geqslant \beta_s \geqslant \gamma_s$. For incompressible flow $\alpha_s + \beta_s + \gamma_s = 0$ and consequently s^* is bounded by ± 1. In addition, the p.d.f. of s^* is uniform for a Gaussian random velocity field. The term s^* can be interpreted as a direct measure of the 'shape' of the deformations caused by the strain-rate tensor. For example, axisymmetric extension occurs when $s^* = 1$, plane shear occurs when $s^* = 0$, and axisymmetric contraction occurs when $s^* = -1$. Lund & Rogers (1994) show that the most probable strain-state in isotropic turbulence is axisymmetric extension, and that this configuration is particularly well correlated with regions of high dissipation.

From our recent study on the scale and geometry relationships in the filtered turbulence (Tao *et al.* 1999*a*, 2000), the following characteristics have been observed: (i) In agreement with trends of unfiltered turbulence observed by Ashurst *et al.* (1987), Vincent & Meneguzzi (1994) and Tsinober *et al.* (1992), there is a preferential alignment between the filtered vorticity and the intermediate eigenvector of the filtered strain-rate tensor. This trend can be explained in the context of restricted Euler dynamics considered in Cantwell (1992) for unfiltered turbulence, and in Chertkov, Pumir & Shraiman (1999) for inertial-range scales. (ii) The vorticity is most probably perpendicular to the most extensive SGS stress eigenvector. (iii) In agreement with Lund & Rogers (1994), the most probable fluid element deformation is axisymmetric extension. (iv) The most probable angle between the eigenvectors of the most extensive stress and the most contracting filtered strain-rate is about 34°, in contrast to typical eddy viscosity models. Our initial impression (Tao *et al.* 2000), which was based on fewer data and less sophisticated analysis, was that the orientations of the other two stress eigenvectors (intermediate and most contracting) were structureless and random. However, as the present paper shows, statistically significant trends can be identified in these other directions as well.

Based on the newly expanded HPIV database, the present paper substantially extends our original analysis by examining the structure of the SGS stress tensor as well as its alignment relative to the filtered strain-rate tensor and the tensor defined by the nonlinear model (1.6). To study the eigenvalue structure of the stress tensor, we introduce a 'stress state parameter', s_τ^*, (which is analogous to s^*), for the deviatoric part of τ_{ij}. To properly characterize the relative orientation of the SGS stress tensor with the filtered strain-rate tensor and the nonlinear model, we introduce the joint p.d.f. of three angles between corresponding eigenvectors. Furthermore, through conditional sampling, we examine the effects of strain-rate magnitude, vorticity magnitude, dissipation and strain and stress state parameters on the alignment trends.

Conditional sampling has been proved to be an effective method for isolating particular features of the turbulent flow in a statistically meaningful fashion (Adrian

1990; O'Neil & Meneveau 1997; Meneveau & Katz 1999*a*; Porté-Agel *et al.* 2000). Such an approach is central to the idea of SGS modelling that has to rely on relating τ_{ij} to spatially localized properties of the resolved scales. For example, we may suspect that high strain rate and/or high vorticity affect the spatial alignment trends and magnitude of the SGS stress tensor. Therefore, it is of interest to isolate regions of large straining and high vorticity which are identified, respectively, by large values of $|\tilde{\boldsymbol{S}}| = (2\tilde{S}_{ij}\tilde{S}_{ij})^{1/2}$ and $|\tilde{\boldsymbol{\omega}}|$. As will be demonstrated in this paper, these parameters do affect the alignment and structure of SGS stresses. Conditional sampling based on s^*, s^*_τ and Π also provides useful information on the relationships between the local flow and stress structures. Conditional sampling is also used in optimal formulations of LES (Langford & Moser 1999) and renormalization group theories (McComb & Watt 1990). Connections between such statistical formulations and the geometric alignment trends studied in the present paper have not yet been explored. Knowledge about eigenvector alignment trends is also important for a new class of models recently proposed by Domaradzki & Saiki (1997), Scotti & Meneveau (1999), and Misra & Pullin (1997).

The experimental set-up and optical instrumentation as well as general flow characterization are described in § 2. Section 3 examines the eigenvalue structures of the filtered strain-rate, SGS stress and modelled stress tensors, as well as their impact on the dissipation by conditional sampling based on Π. Using joint p.d.f.s, § 4 describes the tensor alignment of the SGS stress relative to the filtered strain-rate tensor and the nonlinear model. In § 5, conditional sampling based on Π, $|\tilde{\boldsymbol{S}}|$, s^*_τ, s^* and $|\tilde{\boldsymbol{\omega}}|$ is used to highlight the effects of these parameters on the tensor alignments reported in § 4. A summary and a discussion of the present results are presented in § 6. Specifically, we address effects of the mean flow on the observed alignment trends as well as the impact of the structure and relative alignment between stress and strain-rate tensors on the SGS dissipation. We also explain some of the observed alignment trends using dynamical and kinematical arguments. The paper concludes with ideas for future data analysis.

2. Experimental set-up and general flow characterization

2.1. *Facility*

A schematic description of the closed-loop, test facility is presented in figure 1(*a*). The water flow is driven by a 1.5 kW pump and the velocity measurements are performed within a vertical, square duct with a width, H, of 57.15 mm. Neutrally buoyant (specific weight 1.05), 20 μm diameter polystyrene tracer particles are seeded at a concentration of about $4 \sim 8\,\mathrm{mm}^{-3}$. The test section is located $36H$ downstream of the duct inlet, where conditions close to a fully developed turbulent flow are established. The walls of the test section are made of flush-mounted glass windows, allowing an unobstructed view of a $57.25 \times 57.25 \times 45\,\mathrm{mm}^3$ volume. The centreline mean velocity $\bar{u}_c$ is $2.1\,\mathrm{m\,s}^{-1}$ and the Reynolds number, based on H and $\bar{u}_c$, $Re_H = 1.2 \times 10^5$. Since the wall stress was not measured directly, we estimate the friction factor from Prandtl's friction law for turbulent pipe flows (see. e.g. Schlichting 1979), and obtain a friction velocity of $u_\tau \approx 0.083\,\mathrm{m\,s}^{-1}$ and a friction velocity Reynolds number of $Re_\tau = u_\tau(\frac{1}{2}H)/\nu \approx 2360$. Consequently, the $y^+ = 1$ location is at $y = \nu/u_\tau \approx 0.012\,\mathrm{mm}$.

2.2. *Instrumentation*

This paper provides only a brief description of our HPIV system. Further details on the image acquisition and subsequent data analysis procedures can be found in

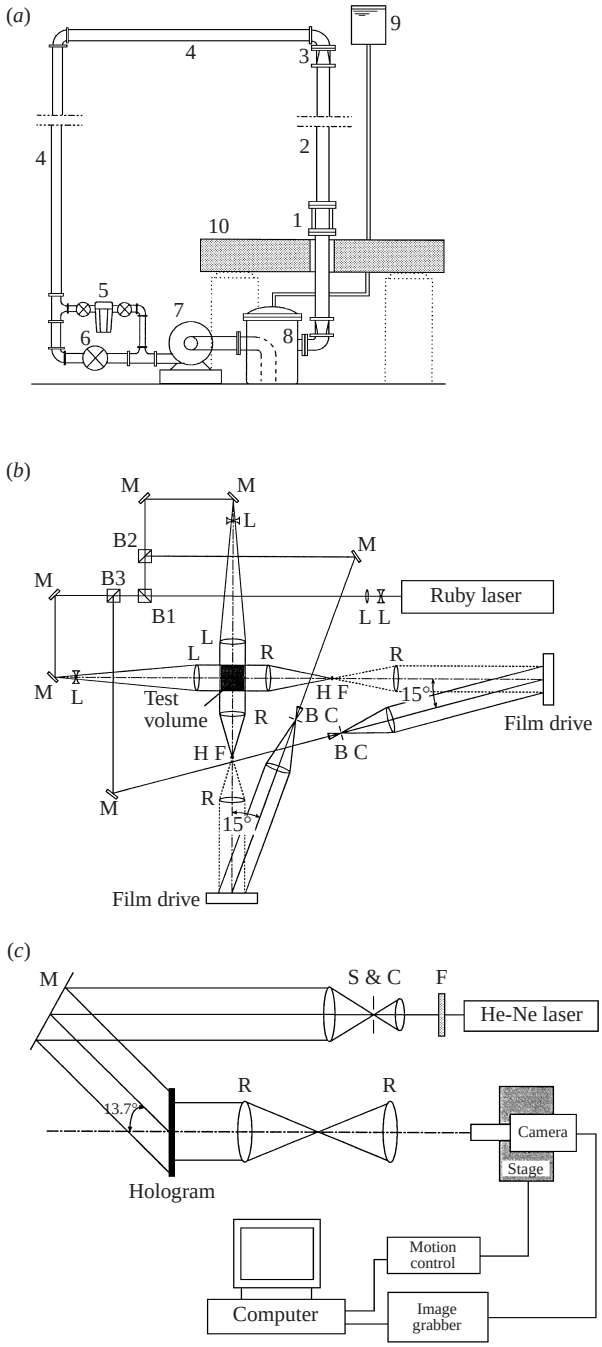

FIGURE 1. Schematic of experimental set-up. (*a*) Test facility for velocity measurement of a turbulent duct flow. 1, optical windows; 2, square channel; 3, entrance; 4, pipe line; 5, filter; 6, valves; 7, pump; 8, tank; 9, pressure head reservoir; 10, optical table. (*b*) Optical set-up for recording two doubly-exposed, off-axis holograms. The duct axis is normal to the page. Forward scattering and optical high-pass filters are used to improve the signal-to-noise ratio of the particle images. B, beam splitter; BC, beam collimator; HF, high-pass filter; L, lens; M, mirror; R, relay lens. (*c*) Hologram reconstruction and image acquisition system. F, neutral density filter; M, mirror; R, relay lens; S & C, Spatial filter and collimator.

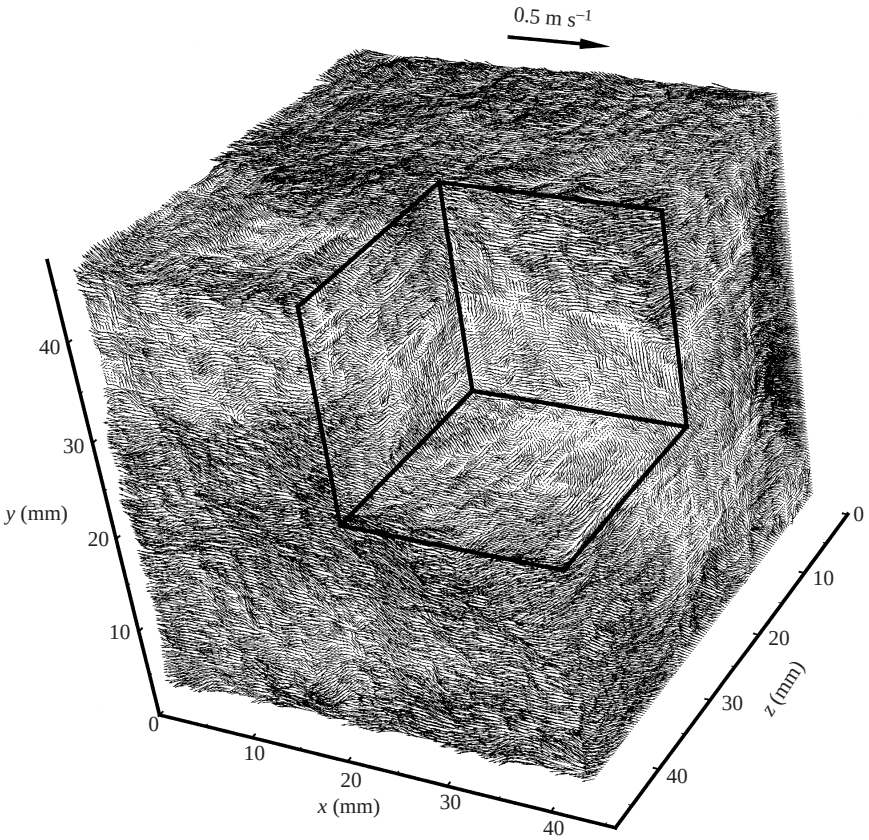

FIGURE 2. A sample three-dimensional, instantaneous velocity distribution in a turbulent duct flow measured by HPIV. The mean flow is along the x-axis, which is also indicated by the reference vector at the top of the figure. The centreline mean velocity, $\bar{u}_c$, has been subtracted from each velocity vector.

Zhang *et al.* (1997). A schematic layout of the optical set-up for recording holograms is shown in figure 1(*b*). Two perpendicular, double exposure holograms delayed by 60 μs are recorded simultaneously. Each hologram is used to determine the two velocity components that are normal to the optical axis. After completing the analysis (see below) the two data sets are combined to form the three-dimensional velocity field. The holograms are developed and then reconstructed using the set-up shown in figure 1(*c*). Each reconstructed three-dimensional image is scanned with a video-microscope mounted on an automated three-axis stage, digitized at a resolution of 4.9 μm pixel^{-1}, enhanced, and compressed without loss of detail. In-house developed software (Roth & Katz 2001) is used for computing the velocity. However, the autocorrelation function is computed directly from the compressed data, a procedure that enables us to improve the computation speed, and maintain high magnification without paying the penalty for a large database (Tao, Malkiel & Katz 1999*b*). The interrogation window size is 192×192 pixel^2 (0.93×0.93 mm^2). With 65% overlap between windows, each data set contains $136 \times 130 \times 128$ vectors with a spacing of $\delta = 0.33$ mm between them. A sample vector map is presented in figure 2. The total size of an average data cube is $46.5 \times 45.1 \times 44.5$ mm^3 and the distance from the duct walls to the data cube boundaries is about 5.6 mm, i.e. about 460 wall units.

The typical displacement between two exposures of tracer particles close to the centre of the duct is about 126 μm (26 pixels). Using a conservative estimate for the

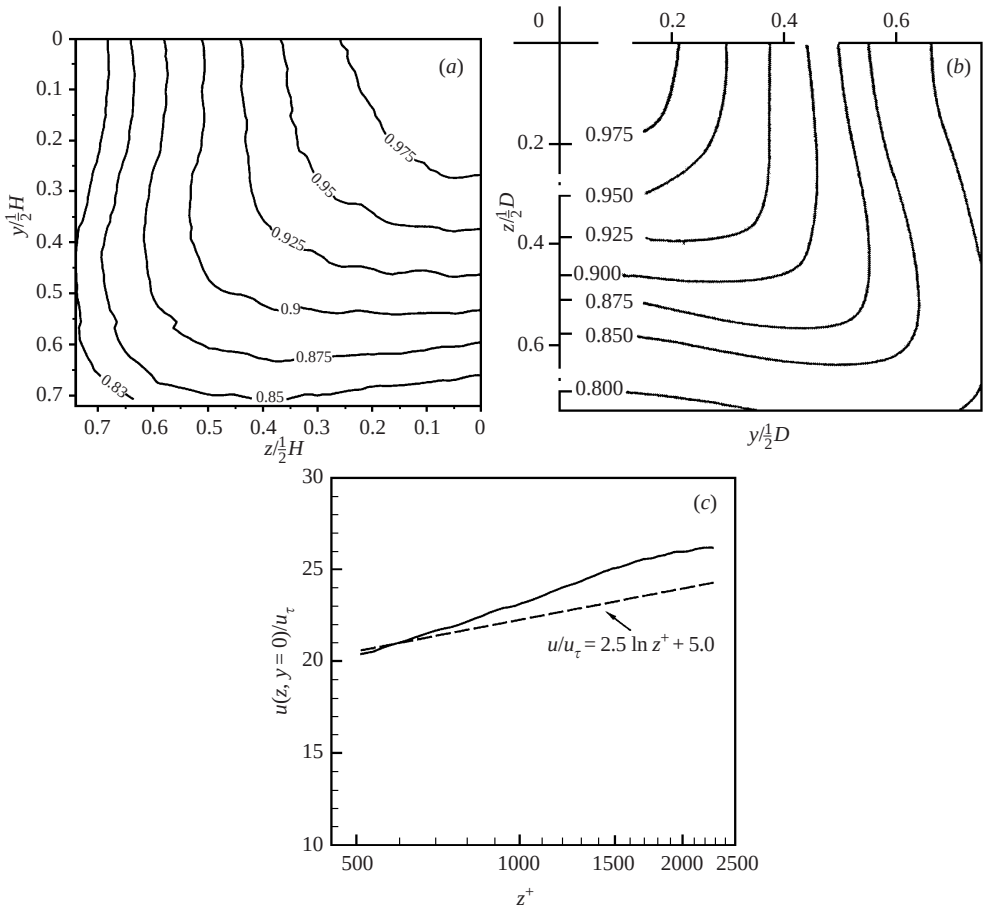

FIGURE 3. (*a*) A contour plot of the ensemble-averaged axial velocity, $\bar{u}(y, z)/\bar{u}_c$. Data is averaged in the streamwise direction, over the four quadrants of the cross section, and over the nine realizations. The origin is located at the centre of the duct and only a combined quadrant is shown. (*b*) A mean axial velocity distribution measured by LDV from Melling & Whitelaw (1976), at $Re_D = 4.2 \times 10^4$ and $x/D = 37$ [reproduced with permission from Cambridge University Press]. Here, D is the hydraulic diameter of a rectangular duct ($41 \times 40\,\text{mm}^2$), and $\bar{u}(y, z)$ is normalized by the bulk velocity. (*c*) Mean axial velocity profile in wall units, evaluated from (*a*) along the z-direction at $y = 0$. Here z^+ increases towards the duct centre.

measurement uncertainty (twice the standard deviation of the difference between real and measured displacement, see Roth, Hart & Katz 1995), the experimental uncertainty for the velocity is estimated at 0.4 pixels, i.e. less than 2%. Consequently, the characteristic uncertainty for the filtered velocity gradients is estimated at 15%. Nine such instantaneous velocity fields, recorded with large delays between them (i.e. statistically independent samples), have been analysed. The results presented in this paper are based on the data from all nine distributions.

2.3. *Data analysis procedure and basic flow characterization*

2.3.1. *General flow characterization*

The mean axial velocity distribution, $\bar{u}(y, z)$, normalized by $\bar{u}_c$, the centreline mean velocity, is presented in figure 3(*a*) as contours of iso-velocity lines. It is averaged along the mean flow direction and over four quadrants of the duct cross-section, in addition to ensemble averaging over the nine instantaneous vector maps. Even though the

large-scale turbulence is not statistically converged with so few data sets, a fair degree of symmetry is observed. Furthermore, the influence of the secondary flow is evident from the bulging of iso-velocity lines towards the duct corner. This distribution is compared and appears to be qualitatively similar to the LDV measurements of Melling & Whitelaw (1976) at a slightly lower Reynolds number (figure 3*b*). Figure 3(*c*) shows the mean velocity profile in wall units, evaluated along the z-direction at $y = 0$ from the contour map of figure 3(*a*). It is evident that present data are essentially confined to the wake region of the duct flow. Recall that the logarithmic layer normally extends to about 10–20% of the distance to the centreline, which in the present case corresponds to a distance up to $z \approx 0.2(\frac{1}{2}H)$ (or $z^+ \approx 500$).

Because the data are not statistically converged for the large scales of turbulence, the r.m.s. distributions of u', v' and w' are patchy, and are not presented here. Still, the distribution of v' and w', the r.m.s. values of velocity fluctuations normal to the mean flow, are fairly uniform, varying between 3.5% and 5% of $\bar{u}_c$ for most of the duct cross-section, with slightly higher values in the perimeter. The values of u' are higher, in general, in a significant portion of the duct, exceeding 8.5% of $\bar{u}_c$ in regions close to the boundaries. In the central portion of the duct, for example the central $5 \times 5\,\mathrm{mm}^2$, u' drops to about the same level as that of v' and w'. Thus, for the central portion of the duct, the fluctuating velocities appear to be fairly isotropic, at least in magnitude. These turbulence intensities are comparable to the measurements reported by Melling & Whitelaw (1976).

One-dimensional turbulence spectra are computed along the mean flow direction (x) and are shown in figure 4. They are computed by subtracting the mean velocities from the three velocity components along the x-direction, de-trending the data by creating a series of first-order derivatives, applying a Welch windowing function, before performing the fast Fourier transformation. For the purpose of examining the data, the results are averaged in the y- and z-directions over the more isotropic central $5 \times 5\,\mathrm{mm}^2$ area. When $k_1 > 400\,\mathrm{rad\,m^{-1}}$, all the three spectra coalesce. At $k_1 > 1300\,\mathrm{rad\,m^{-1}}$, they appear to have, at least in part, a $-\frac{5}{3}$ slope, even though this range spans less than half a decade. For $k_1 > 4000\,\mathrm{rad\,m^{-1}}$, the slope of the spectra increases, indicating that the present data extend into the dissipative range. The spectra level off towards the very end of the high wavenumber range ($k_1 > 6700\,\mathrm{rad\,m^{-1}}$), where they are obscured by the measurement noise, a phenomenon commonly encountered in PIV data (Liu *et al.* 1994, 1999; Eggeles *et al.* 1994).

Using these data, we obtain the Taylor micro-scale Reynolds number, $Re_\lambda = u'\lambda/\nu$, to be about 260. It is estimated from $\lambda \approx u'(15\nu/\varepsilon)^{1/2} \approx (15\nu l/u')^{1/2} \approx 3.3\,\mathrm{mm}$, where u' is the estimated r.m.s. value of the streamwise velocity fluctuations ($\approx 0.08\,\mathrm{m\,s^{-1}}$) along the duct centreline and l is the integral scale, estimated as $l \approx H$. Estimating the Kolmogorov scale, η, from $\eta \approx (\nu^3 l/u'^3)^{1/4}$, we obtain $\eta \approx 100\,\mu\mathrm{m}$. Notice that the integral scale used here is only an order of magnitude estimate. As will be shown later, the resulting estimate for the dissipation rate, $\varepsilon \approx u'^3/l \approx 9.0 \times 10^{-3}\,\mathrm{m^2\,s^{-3}}$, is of the same order of magnitude as (but lower than) the SGS dissipation rate calculated directly from the data.

2.3.2. *The filtered turbulence*

Three-dimensional spatial filtering of the velocity field is performed according to

$$\left.\begin{aligned} \tilde{u}_i(\boldsymbol{x}) &= \int_{-\infty}^{\infty}\int_{-\infty}^{\infty}\int_{-\infty}^{\infty} u_i(\boldsymbol{x}')F_\Delta(\boldsymbol{x}-\boldsymbol{x}')\mathrm{d}^3\boldsymbol{x}', \\ F_\Delta(\boldsymbol{x}) &= \begin{cases} \Delta^{-3} & \text{when } |\boldsymbol{x}| \leqslant \frac{1}{2}\Delta \\ 0 & \text{when } |\boldsymbol{x}| > \frac{1}{2}\Delta, \end{cases} \end{aligned}\right\} \tag{2.1}$$

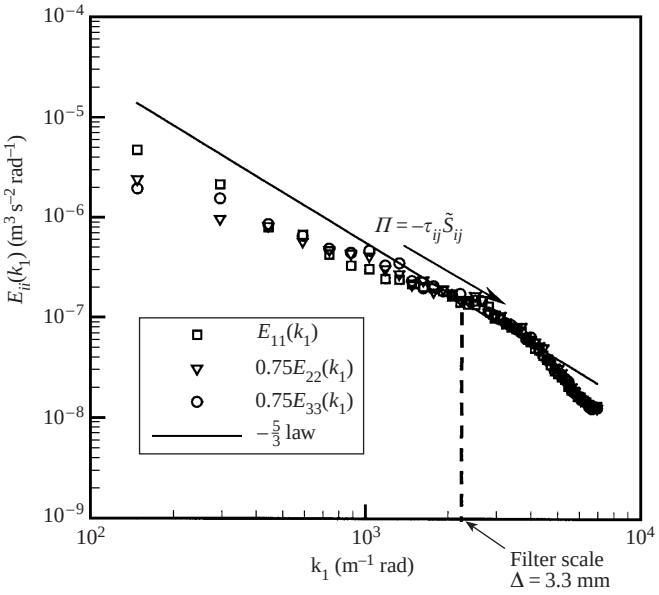

FIGURE 4. One-dimensional (streamwise) turbulent spectra. Data are calculated over the central portion of the duct ($5 \times 5\,\mathrm{mm}^2$) and also averaged over the nine instantaneous realizations. The highlighted wavenumber corresponds to the scale of the spatial filter used in the subsequent analyses.

where $F_\Delta(\boldsymbol{x})$ is a spatial, low-pass box filter with scale Δ. In the present work, we choose Δ equal to 10 vector spacings, i.e. $\Delta = 10\delta = 3.3\,\mathrm{mm}$. As indicated in figure 4, this value corresponds to a wavenumber inside the limited inertial range of the turbulence spectra. The skewness and kurtosis of the streamwise derivative of filtered velocity are, $S_\Delta \approx -0.36$ and $K_\Delta \approx 3.8$. The value of S_Δ is consistent with results of Cerutti, Meneveau & Knio (2000) who obtained S_Δ between -0.4 and -0.3 (as opposed to -0.5 for unfiltered turbulence).

The subgrid-scale stress, τ_{ij}, is computed according to its definition (1.1), and S_{ij} and $\tilde{\omega}_i$ are computed directly from filtered velocity derivatives using second-order finite difference ((1.2) and (1.3)). To be consistent with simulations, as recommended in Liu *et al.* (1994), we calculate the derivatives on a grid of size Δ instead of the original velocity grid. After the local quantities, such as $\tilde{S}_{ij}$, are computed, the reference point for the coarse mesh (scale Δ) is shifted by δ ($\delta = 330\,\mu\mathrm{m}$) of the finer measurement grid in order to enlarge the database and obtain improved statistics. In order to evaluate the modelled SGS stress using the similarity model (1.5), the velocity field has to be filtered again at a scale 2Δ. The parameters of this twice-filtered velocity field are calculated by using only the resulting coarse grid with vector spacing of 2Δ, similar to the procedures performed at Δ. All the relevant statistics are calculated for each grid point sampled with proper offset from the data boundaries.

Figure 5(*a*) shows the p.d.f. of Π, $|\tilde{\boldsymbol{S}}|$, $|\boldsymbol{\omega}|$, and $|\boldsymbol{\tau}|(=\tau_{ij}^d\tau_{ij}^d)^{1/2}$, and $\tau_{ij}^d = \tau_{ij} - \tau_{kk}\delta_{ij}/3$) obtained from the nine instantaneous velocity distributions. Note that the p.d.f. of Π has the typical negative tail indicating energy backscatter (see for example, Meneveau & Katz 1999*a*). However, the asymmetry of the curve leads to a positive mean SGS dissipation, $\Pi_{mean} = 2.46 \times 10^{-2}\,\mathrm{m}^2\,\mathrm{s}^{-3}$. This value is larger than, but of the same order of magnitude as, ε ($\approx 9.0 \times 10^{-3}\,\mathrm{m}^2\,\mathrm{s}^{-3}$), the energy dissipation rate estimated in § 2.3.1. The p.d.f. of $|\boldsymbol{\tau}|$, exhibiting a small mode but a long tail, has a distinctively different shape from those of $|\tilde{\boldsymbol{S}}|$ and $|\tilde{\boldsymbol{\omega}}|$. The other normalizing parameters, i.e. the r.m.s.

values of strain-rate, vorticity, and SGS stress are $\sigma_{|\tilde{\mathbf{S}}|} = 14.03\,\mathrm{s}^{-1}$, $\sigma_{|\tilde{\boldsymbol{\omega}}|} = 16.39\,\mathrm{s}^{-1}$, and $\sigma_{|\boldsymbol{\tau}|} = 2.16 \times 10^{-3}\,\mathrm{m}^2\,\mathrm{s}^{-2}$, respectively.

To calculate the magnitude and orientation of eigenvectors of the filtered strain-rate and SGS stress tensors, the measured tensors are diagonalized. Probability density functions of the eigenvalues of τ_{ij}^d and $\tilde{S}_{ij}$, are presented in figures 5(b) and 5(c), respectively. Here, α_s, β_s and γ_s are the most extensive, intermediate and most contracting eigenvalues of $\tilde{S}_{ij}$, respectively. Similarly, $\alpha_{-\tau}$, $\beta_{-\tau}$ and $\gamma_{-\tau}$ are, respectively, the most extensive, intermediate, and most contracting eigenvalues of the negative SGS stress, $-\tau_{ij}^d$. In the same order, they simultaneously correspond to the most contracting, intermediate (with opposite sign) and most extensive eigenvalues of τ_{ij}^d, i.e. $\alpha_{-\tau} = -\gamma_\tau$, $\beta_{-\tau} = -\beta_\tau$ and $\gamma_{-\tau} = -\alpha_\tau$. In accordance with these definitions, we also set $\boldsymbol{\alpha}_s$, $\boldsymbol{\beta}_s$ and $\boldsymbol{\gamma}_s$ to be, respectively, unit vectors aligned with the most extensive, intermediate and most contracting eigenvectors of $\tilde{S}_{ij}$, while $\boldsymbol{\alpha}_{-\tau}$, $\boldsymbol{\beta}_{-\tau}$ and $\boldsymbol{\gamma}_{-\tau}$ are unit vectors aligned with the most contracting, intermediate and most extensive eigenvectors of τ_{ij}^d. Figure 5(b) shows that $\beta_{-\tau}$ is mostly negative and that the most extensive stress ($\gamma_{-\tau}$) extends to higher magnitudes than the most contracting stress. As is evident from figure 5(c), the most probable β_s is positive but its value extends to the positive and negative range. The most contracting strain-rate eigenvalue (γ_s) extends to higher magnitudes than the most extensive strain.

3. Eigenvalue structures of filtered strain-rate and SGS stress tensors

The p.d.f.s shown in figures 5(b) and 5(c) do not fully characterize the joint distributions of the three eigenvalues. Since they sum to zero, only two are independent. Furthermore, a single parameter can be defined by proper normalization, as was done for the strain-rate tensor by Lund & Rogers (1994). In analogy to s^* (1.8), in § 3.1, we introduce a 'stress state parameter', s_τ^*. Single and joint p.d.f.s of s^* and s_τ^* are used to characterize the most probable states of the strain-rate and stress fields. The eigenvalue structure of the nonlinear/similarity models is also examined and compared to that of τ_{ij}^d. In § 3.2, we examine the effects of s^* and s_τ^* on the SGS dissipation.

3.1. *Probability density functions of s^* and s_τ^**

To characterize the structure of the SGS stress tensor we introduce a dimensionless parameter, s_τ^*, for the deviatoric stress τ_{ij}^d. Its definition is

$$s_\tau^* = -3\sqrt{6}\alpha_\tau\beta_\tau\gamma_\tau/(\alpha_\tau^2 + \beta_\tau^2 + \gamma_\tau^2)^{3/2} = 3\sqrt{6}\alpha_{-\tau}\beta_{-\tau}\gamma_{-\tau}/(\alpha_{-\tau}^2 + \beta_{-\tau}^2 + \gamma_{-\tau}^2)^{3/2} = -s_{-\tau}^*. \tag{3.1}$$

By construction, $\alpha_{-\tau} \geqslant \beta_{-\tau} \geqslant \gamma_{-\tau}$ and $\alpha_{-\tau} + \beta_{-\tau} + \gamma_{-\tau} = 0$. Thus, like s^*, s_τ^* is within the range ± 1. The p.d.f.s of s^* and s_τ^* indicate the relative abundance of specific states, i.e. specific ratios between magnitudes of the filtered strain-rate and SGS stress eigenvalues, respectively. Moreover, in order to draw meaningful conclusions, we demonstrate (see below) that the p.d.f.s of s^* and s_τ^* are not biased towards particular states when tested using Gaussian random fields.

Figure 6 shows the p.d.f.s of s^* and s_τ^*. As suggested in Lund & Rogers (1994), in calculating the p.d.f. of s^*, the dilatational error of the strain-rate tensor is isotropically removed so that $\tilde{S}_{ij}$ remains trace-free. Also shown in figure 6 are p.d.f.s computed from four randomly generated velocity fields, each containing 128^3 vectors (each velocity component is chosen from a uniform distribution independently, creating a white noise in space). The distributions of $P(s^*)$ and $P(s_\tau^*)$ computed

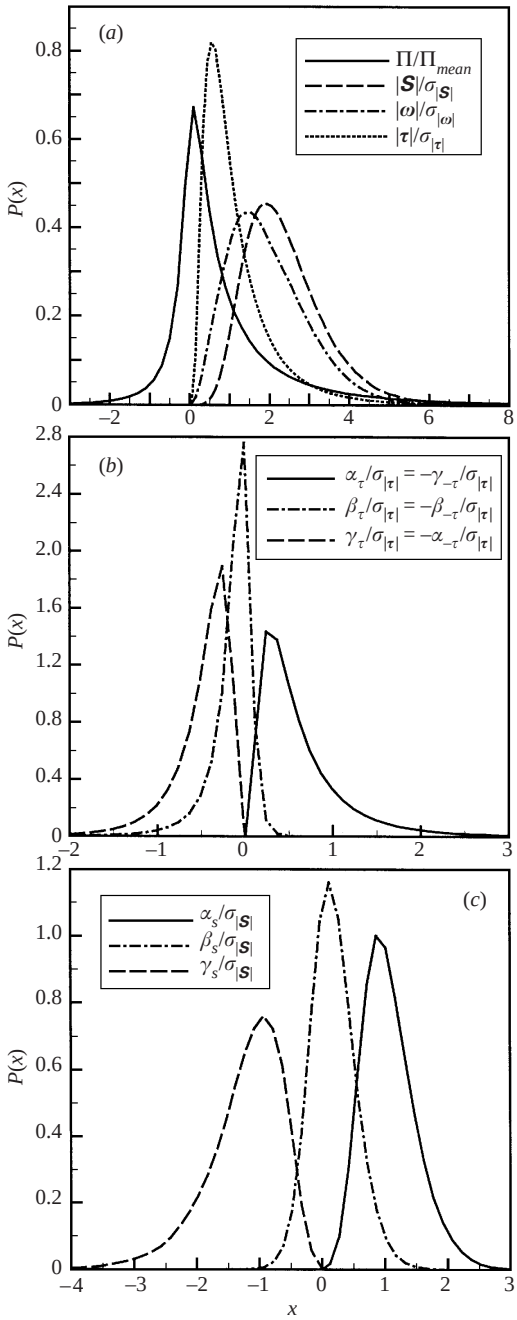

FIGURE 5. Probability density function of (*a*) SGS dissipation, filtered vorticity, filtered strain-rate and the deviatoric SGS stress magnitudes, (*b*) eigenvalues of the deviatoric SGS stress tensor, and (*c*) eigenvalues of the strain-rate tensor.

using the random velocity field are essentially flat, although $P(s_\tau^*)$ has a slightly elevated probability towards -1. This negligible bias may be attributed to the fact that the SGS stress is a quadratic functional of the velocities. Consistent with the observations of Lund & Rogers (1994), the most probable strain state is at $s^* = 1$,

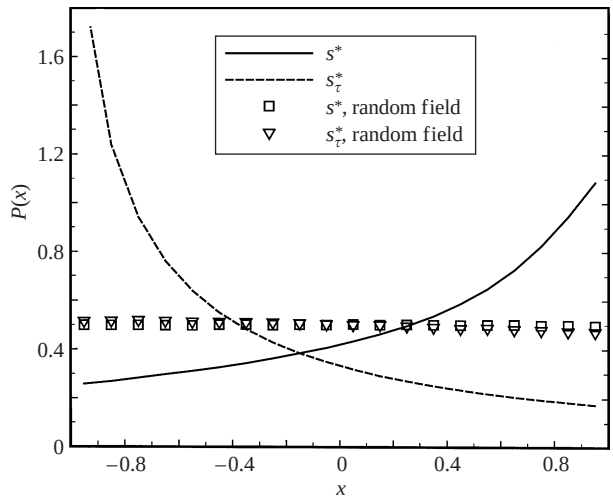

FIGURE 6. Probability density function of the strain state and stress state parameters s^* and s^*_τ evaluated from the measured turbulent velocity field and a random field of uniform distribution.

corresponding to an eigenvalue ratio of $\alpha_s : \beta_s : \gamma_s = 1 : 1 : -2$. The associated local flow structure is axisymmetric extension (more complete characterizations could be achieved with joint p.d.f.s of two eigenvalues, but for now we restrict our attention to characterization based on a single dimensionless parameter). The most probable stress state, on the other hand, is at $s^*_\tau = -1$, corresponding to an eigenvalue ratio of $\alpha_\tau : \beta_\tau : \gamma_\tau = 2 : -1 : -1$ (or $\alpha_{-\tau} : \beta_{-\tau} : \gamma_{-\tau} = 1 : 1 : -2$). Thus, the preferred state/structure of the stress tensor is also axisymmetric, but it is axisymmetric contraction. Considering that in eddy-viscosity models the tensors have opposite sign (see (1.4)) the inversion may not be surprising. However, the probability of $s^*_\tau = -1$ is substantially higher than the probability of $s^* = 1$. We will return to this issue while presenting the joint p.d.f.s.

To evaluate how the similarity ((1.5), with the second filter at scale 2Δ, following Liu *et al.* 1994) and the nonlinear (1.6) models predict the preferred stress state, p.d.f.s of s^{*sim}_τ and s^{*nl}_τ computed from the modelled stress fields are plotted in figure 7. Both models generate essentially the same p.d.f., consistent with the fact that the nonlinear model can be interpreted as a first-order approximation of the similarity model. Both also predict the high probability of $s^*_\tau = -1$, but they over-emphasize the preferred stress state by a large margin. In fact, it seems that the models prescribe the $2 : -1 : -1$ ratio (for $\alpha_\tau : \beta_\tau : \gamma_\tau$) or values close to it to almost the entire field.

In an attempt to determine whether this trend is unique to our experimental data, we repeat the analysis using DNS data of isotropic turbulence at $Re_\lambda \approx 93$ that is available from Cerutti & Meneveau (1998). As shown in figure 7, the same trend occurs. In both cases the nonlinear (or similarity) model 'over predicts' the frequency of occurrence of the $2 : -1 : -1$ state.

The joint p.d.f., $P(s^*, s^*_\tau)$, presented in figure 8(a), shows the relationship between the structures of the strain-rate and the stress tensors. The overall p.d.f. peak is located at $s^* = 1$ and $s^*_\tau = -1$. Thus, the combined most probable strain and stress structures are axisymmetric extension in the strain-rate field and axisymmetric contraction in the stress field. However, figure 8(a) also shows that $s^*_\tau = -1$ is the most likely stress state for any value of s^* and that $s^* = 1$ is the most likely strain state for any s^*_τ. Hence, a

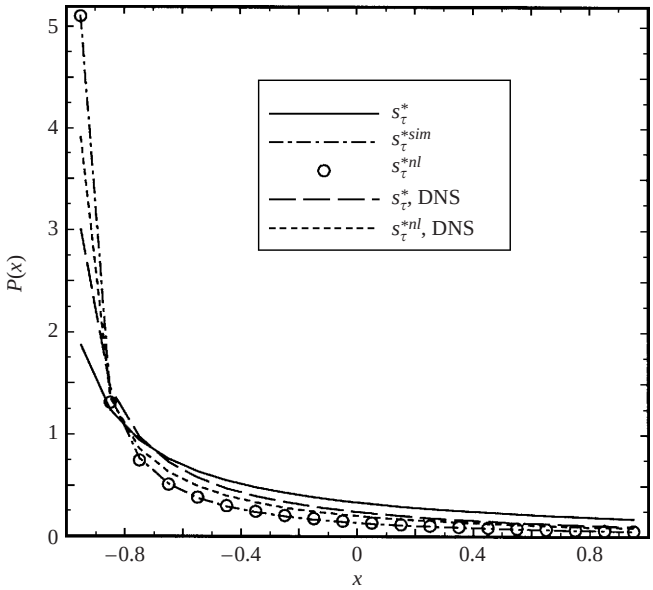

FIGURE 7. Probability density function of the stress parameter s_τ^*, evaluated from the measured and model stresses, and from a DNS result of an isotropic turbulence at $Re_\lambda \approx 93$.

certain configuration of the filtered strain-rate eigenvalues does not imply a similar, reciprocal configuration of the SGS stress eigenvalues. This trend is a contradiction to eddy viscosity models, for which the joint p.d.f. would be concentrated along the line $s_\tau^* = -s^*$, and is consistent with the poor local agreement between τ_{ij}^d and $\tilde{S}_{ij}$ usually observed in *a priori* tests.

To compare the structure of the nonlinear/similarity stresses to that of τ_{ij}^d, figure 8(*b*) shows the joint p.d.f. of $P(s_\tau^*, s_\tau^{*nl})$. As before, the tensor is made traceless by subtracting $\frac{1}{3}\tau_{kk}^{nl}\delta_{ij}$. The distribution of $P(s_\tau^*, s_\tau^{*sim})$ is not shown since its behaviour is very similar to the nonlinear model. Consequently, we will hereinafter focus on the nonlinear model in evaluating the structure of 'similarity type' models. Compared to $P(s^*, s_\tau^*)$, $P(s_\tau^*, s_\tau^{*nl})$ has a much higher (4.5 times higher) p.d.f. peak at $s_\tau^* = -1$ and $s_\tau^{*nl} = -1$. Also, s_τ^{*nl} tends to -1 much more likely than s_τ^* to -1. Finally, for every value of s_τ^*, the most probable value of s_τ^{*nl} is still -1 and, for every value of s_τ^{*nl}, the most probable s_τ^* is -1. This trend indicates that the stress state of the nonlinear model is also decoupled from that of the measured stresses, whereas a perfect (in an *a priori* sense) model would have a peak along the $s_\tau^* = s_\tau^{*nl}$ line.

In summary, the eigenvalue structures determined by eddy viscosity and similarity models do not predict the structure (state) of the SGS stress tensor. However, they both point to the correct most probable state. The eddy viscosity model underpredicts the probability and the similarity model overprescribes it. Similar to the conclusions in Liu *et al.* (1999), these opposing trends may further support a mixed model.

3.2. *Relationships between SGS dissipation, s^*, s_τ^*, and magnitudes of $|\tilde{\boldsymbol{S}}|$ and $|\tilde{\boldsymbol{\omega}}|$*

In this section, we address how different flow and stress topologies (e.g. axisymmetric extension or contraction) are related to different ranges of SGS dissipation (e.g. strong forward or back scatter). These relationships are quantified using joint p.d.f.s of s^* or s_τ^* and Π. Figure 9(*a*) is a contour map of $P(s^*, \Pi/\Pi_{mean})$, the joint p.d.f. of s^* and Π, and figure 9(*b*) is $P(s_\tau^*, \Pi/\Pi_{mean})$ As is evident, regions of negative dissipation exist

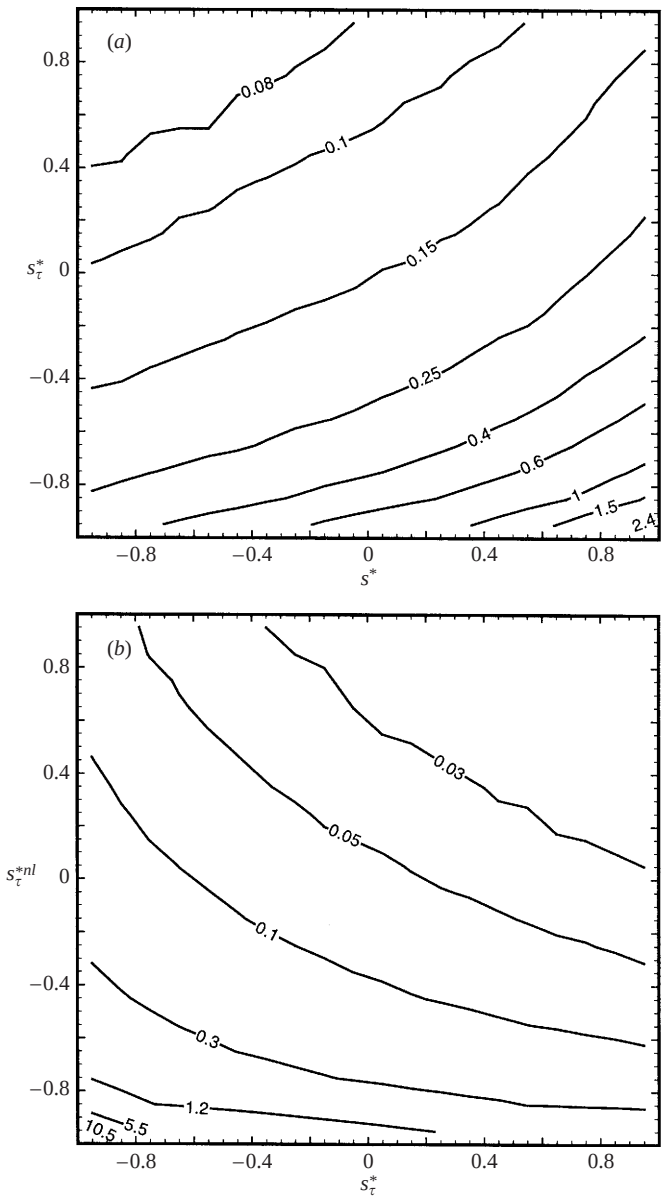

FIGURE 8. Joint p.d.f. of (*a*) s^* and s_τ^*, (*b*) s_τ^* and s_τ^{*nl} by the nonlinear model.

throughout the whole range of both s^* and s_τ^*, but the 'positive' tails are clearly much larger. In both figures 9(*a*) and 9(*b*) and for all values of s^* and s_τ^*, the most probable dissipation is slightly above zero. The range of dissipation levels widens with increasing s^* mostly on the positive side and only very slightly on the negative side. In the p.d.f. involving s_τ^*, the range of dissipation values expands with decreasing s_τ^* both on the positive and negative sides, but still, the range of positive values increases at a faster rate.

Although the magnitudes of peaks differ, the trends in figures 9(*a*) and 9(*b*) in the positive dissipation range are the same for s_τ^* and s^*, but they differ in the negative dissipation range. We conclude that, in regions of high dissipation, the axisymmetric

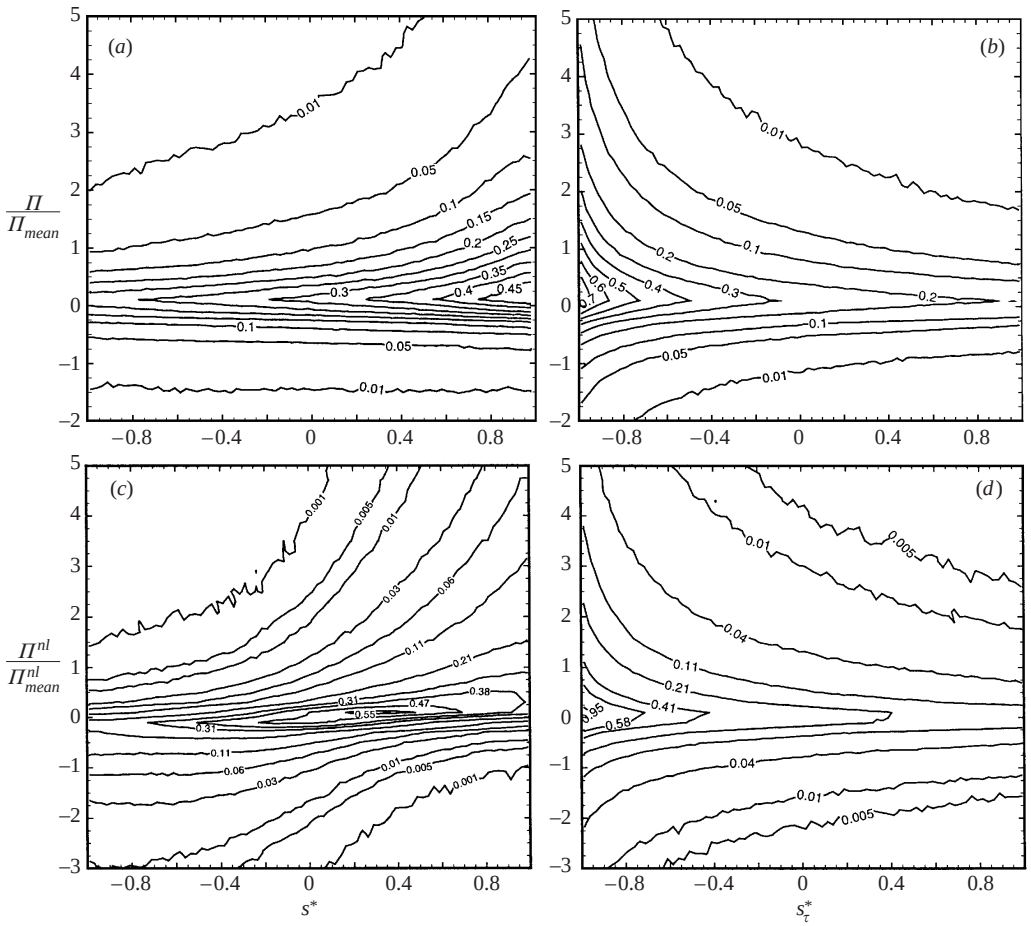

FIGURE 9. Joint p.d.f. of s^* and s^*_τ with the real and nonlinear model dissipation rates: (*a*) s^* and Π, (*b*) s^*_τ and Π, (*c*) s^* and Π^{nl}, (*d*) s^*_τ and Π^{nl}.

extension configuration ($s^* = 1$) is dominant. In regions of low positive dissipation there is only a slight preference towards $s^* = 1$, whereas in regions of high negative dissipation there is no preferred strain state. In contrast to the latter trend, the most probable stress state ($s^*_\tau = -1$) is prominent in regions of both high positive and high negative dissipation.

Prediction of dissipation by the nonlinear model is an important issue, since overprediction of negative dissipation (energy backscatter) may lead to undesirable numerical instabilities. Figures 9(*c*) and 9(*d*) present the joint p.d.f.s of the dissipation estimated using the nonlinear model, i.e. $\Pi^{nl} = -\tau^{nl}_{ij}\tilde{S}_{ij}$, with s^* and with s^*_τ, respectively. τ^{nl}_{ij} is given by (1.6) with $C_{nl} = 0.42$ chosen from the data such that $\Pi^{nl}_{mean} = \Pi_{mean}$. A comparison between figures 9(*a*) and 9(*c*) shows that even if the mean dissipation is matched, the differences in the backscatter region when $s^* < 0$ are substantial. In fact, for $s^* < 0$, the nonlinear model predicts that the p.d.f. peaks are in the negative dissipation range, and the mean dissipation rates are negative (whereas they remain positive for Π of figure 9*a*). Although the most probable strain state is $s^* = 1$, still $s^* < 0$ occurs in more than 30% of the data volume, which means that unless it is corrected,

the nonlinear model overprescribes backscatter in a significant fraction of the flow field, especially in regions of axisymmetric contraction. A comparison between figures 9(*b*) and 9(*d*) shows that the differences are quite small and the peaks are always in the positive range of Π^{nl} and Π. Clearly, trends (of Π^{nl} and Π) with s^* and with s^*_τ are quite different. As noted in § 1.1, the eddy-viscosity term in the mixed model (1.7) is primarily used to increase the dissipation (the Smagorinsky dissipation is, by definition, always positive), and reduce the likelihood of excessive backscatter. However, as will be shown in the Appendix, for regions with $s^* < 0$, this remedy is insufficient.

Next, the effects of strain-rate and vorticity magnitudes are considered. Figure 10 presents joint p.d.f.s of Π with $|\tilde{\boldsymbol{S}}|$ and $|\tilde{\boldsymbol{\omega}}|$. With increasing strain-rate magnitude the iso-probability lines expand both in the positive and negative directions but the expansion rate is higher on the positive side. Thus, for each $|\tilde{\boldsymbol{S}}|/\sigma_{|\tilde{\boldsymbol{S}}|}$ there is a range of dissipation levels that extends from negative to positive values. The insert in figure 10(*a*) shows a log–log plot of the conditional mean dissipation as a function of strain-rate magnitude (indicated by the solid line). It is evident that Π/Π_{mean} increases less rapidly than $[|\tilde{\boldsymbol{S}}|/\sigma_{|\tilde{\boldsymbol{S}}|}]^3$, as the Smagorinsky model would predict, but still, the growth is monotonic. In contrast, predictions of the nonlinear model (Π^{nl} *vs.* $|\tilde{\boldsymbol{S}}|$) show some notable differences (data not shown), especially in regions of high $|\tilde{\boldsymbol{S}}|$, where the model generates considerably higher dissipation in both the positive and negative ranges.

The trends with vorticity (figure 10*b*) are different, notably in regions with low $|\tilde{\boldsymbol{\omega}}|/\sigma_{|\tilde{\omega}|}$. A wide range of dissipation levels already exists and this range expands quickly with increasing $|\tilde{\boldsymbol{\omega}}|/\sigma_{|\tilde{\omega}|}$ both in the positive and negative sides (with higher positive values). Unlike the trends with strain-rate, there is only a mild increase of the most probable dissipation with increasing vorticity and it remains below $\Pi/\Pi_{mean} \approx 1.5$. Thus, the magnitude of vorticity has a weak effect on the statistical distribution of SGS dissipation. However, the joint p.d.f. of Π^{nl} and $|\tilde{\boldsymbol{\omega}}|$ (data not shown) shows that the nonlinear model generates a higher level of negative dissipation over a wide range of vorticity magnitudes.

Finally, in order to characterize the possible relationships between vorticity magnitudes and the SGS stress and filtered strain-rate topologies, we present joint p.d.f.s of $|\tilde{\boldsymbol{\omega}}|$ with s^* and s^*_τ in figure 11. With decreasing s^*_τ and increasing s^*, there is an increasing probability of finding regions with high $|\tilde{\boldsymbol{\omega}}|$. Regions with low $|\tilde{\boldsymbol{\omega}}|$ seem to be uniformly distributed with small variations in p.d.f. of either s^* or s^*_τ. This trend indicates that regions of high $|\tilde{\boldsymbol{\omega}}|$ are well correlated with the preferred strain-rate and stress states. A similar trend is also observed in joint p.d.f.s of $|\tilde{\boldsymbol{S}}|$ with s^* and s^*_τ (data not shown).

4. Geometric alignment statistics of real and modelled stress tensors

This section starts with definitions of angles that are required for characterizing the alignment of an orthogonal tensor in a coordinate system defined by another orthogonal tensor. Then, we provide a detailed account of the relative alignments between the filtered strain-rate, real and modelled (nonlinear) SGS stress tensors.

4.1. *Joint p.d.f. of three angles to fully characterize relative alignment of two tensors*

In our previous study (Tao *et al.* 2000), a two-dimensional joint p.d.f. has been introduced to evaluate the orientation of a vector in a three-dimensional space spanned by orthogonal tensor eigenvectors. As shown in figure 12, defining the orientation of a vector (say $\boldsymbol{\alpha}_{-\tau}$) in the coordinate system spanned by $\boldsymbol{\alpha}_s$, $\boldsymbol{\beta}_s$ and $\boldsymbol{\gamma}_s$ requires two

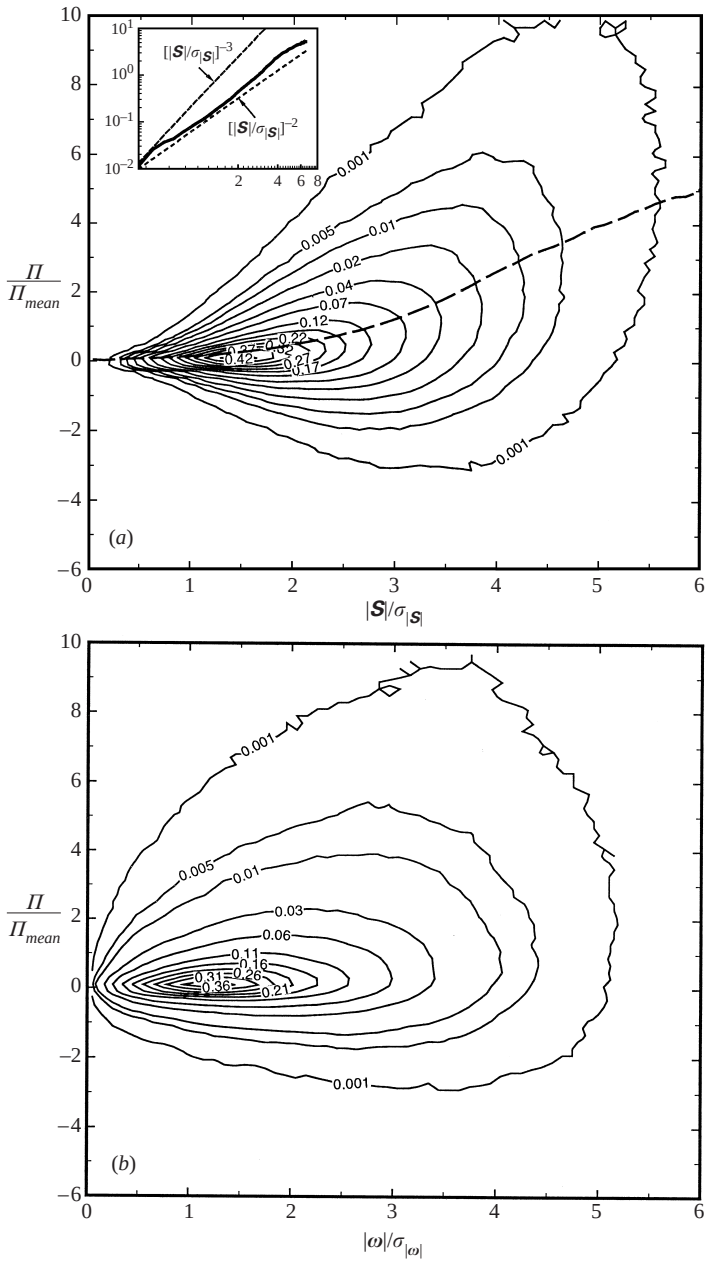

FIGURE 10. Joint p.d.f. of SGS dissipation with (*a*) the strain-rate and (*b*) vorticity. The dashed line in (*a*) indicates the mean SGS dissipation, $\langle \Pi / \Pi_{mean} \rangle$, conditioned on $|\tilde{\boldsymbol{S}}|/\sigma_{|\tilde{\boldsymbol{S}}|}$. The log–log plot in the insert compares the data with the $[|\tilde{\boldsymbol{S}}|/\sigma_{|\tilde{\boldsymbol{S}}|}]^3$ and $[|\tilde{\boldsymbol{S}}|/\sigma_{|\tilde{\boldsymbol{S}}|}]^2$ lines.

angles, for example $\theta(\boldsymbol{\alpha}_{-\tau} - \boldsymbol{\alpha}_s)$ and $\phi(\boldsymbol{\alpha}_{-\tau} - \boldsymbol{\beta}_s)$. In order to present unbiased results, we compute the joint p.d.f.s of $\cos\theta$ and ϕ. With such variables, a randomly aligned vector corresponds to a uniform p.d.f. In this analysis $\cos[\theta(\boldsymbol{\alpha}_{-\tau} - \boldsymbol{\alpha}_s)] = |\boldsymbol{\alpha}_{-\tau} \cdot \boldsymbol{\alpha}_s|$, whereas $\phi(\boldsymbol{\alpha}_{-\tau} - \boldsymbol{\beta}_s)$ is the angle between $\boldsymbol{\beta}_s$ and the projection of $\boldsymbol{\alpha}_{-\tau}$ on the $(\boldsymbol{\beta}_s, \boldsymbol{\gamma}_s)$-plane. This approach has enabled us to quantify the alignment probability of the

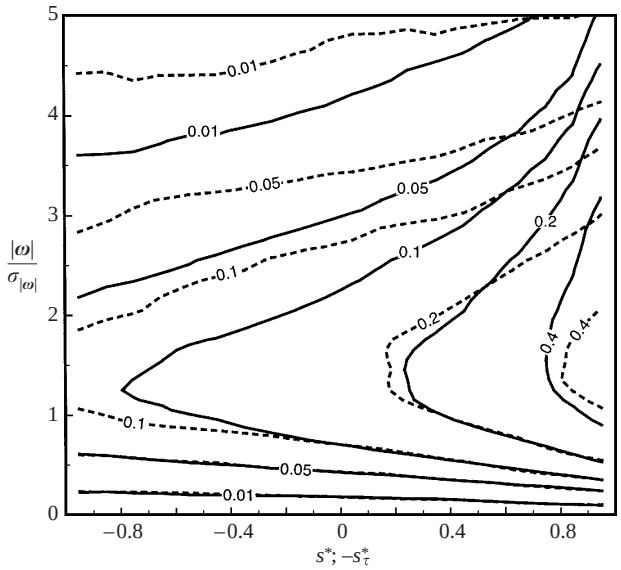

FIGURE 11. Joint p.d.f. of $|\tilde{\boldsymbol{\omega}}|$ with s^*_τ and s^*. ——, $P(|\tilde{\boldsymbol{\omega}}|, s^*_\tau)$; - - -, $P(|\tilde{\boldsymbol{\omega}}|, s^*)$.

vorticity vector relative to the strain-rate tensor ($\tilde{\omega}_i$ is preferentially aligned with $\boldsymbol{\beta}_s$, see § 5.4 for details) and the SGS stress tensor ($\tilde{\omega}_i$ is preferentially perpendicular to $\boldsymbol{\gamma}_{-\tau}$).

However, a two-dimensional joint p.d.f. cannot uniquely characterize the relative alignment between two tensors. To examine the alignment of the full tensor with a single joint p.d.f. it is necessary to define a third angle that would still provide an unbiased three-dimensional joint p.d.f. As before (figure 12), we use the angles $\theta(\boldsymbol{\alpha}_{-\tau} - \boldsymbol{\alpha}_s)$ and $\phi(\boldsymbol{\alpha}_{-\tau} - \boldsymbol{\beta}_s)$ to fully determine the orientation of $\boldsymbol{\alpha}_{-\tau}$. Consequently, the orientation of the $(\boldsymbol{\beta}_{-\tau}, \boldsymbol{\gamma}_{-\tau})$-plane is also determined, but not the directions of $\boldsymbol{\beta}_{-\tau}$ or $\boldsymbol{\gamma}_{-\tau}$ on this plane. We then define an angle $\zeta(\boldsymbol{\gamma}_{-\tau} - \boldsymbol{\gamma}^P_s)$ to determine the direction of $\boldsymbol{\gamma}_{-\tau}$. It is the angle between $\boldsymbol{\gamma}_{-\tau}$ and $\boldsymbol{\gamma}^P_s$ on the $(\boldsymbol{\beta}_{-\tau}, \boldsymbol{\gamma}_{-s})$-plane (i.e. normal to $\boldsymbol{\alpha}_{-\tau}$), where $\boldsymbol{\gamma}^P_s$ is the projection of $\boldsymbol{\gamma}_s$ on this plane. The three angles, θ, ϕ and ζ uniquely define the orientation of all three stress eigenvectors (and as a result, τ^d_{ij}) in a space defined by the eigenvectors of $\tilde{S}_{ij}$. This choice of the third angle preserves the same statistical consistency of our previous study, i.e. when tested against a random white noise velocity field, these variables generate an essentially uniform joint p.d.f. (not shown). Using simpler (i.e. more intuitive) angles, for instance $\theta(\boldsymbol{\gamma}_{-\tau} - \boldsymbol{\gamma}_s)$, together with $\theta(\boldsymbol{\alpha}_{-\tau} - \boldsymbol{\alpha}_s)$ and $\phi(\boldsymbol{\alpha}_{-\tau} - \boldsymbol{\beta}_s)$ leads to a biased (and thus not useful) joint p.d.f. since the latter two angles constrain the range of values that $\theta(\boldsymbol{\gamma}_{-\tau} - \boldsymbol{\gamma}_s)$ can attain.

In the following sections, we use the three-dimensional joint p.d.f. in the form of $P\{\cos[\theta(\boldsymbol{\alpha}_{-\tau} - \boldsymbol{\alpha}_s)], \phi(\boldsymbol{\alpha}_{-\tau} - \boldsymbol{\beta}_s), \zeta(\boldsymbol{\gamma}_{-\tau} - \boldsymbol{\gamma}^P_s)\}$ to quantify the alignment trends of $-\tau^d_{ij}$ relative to $\tilde{S}_{ij}$. In certain illustrations, we use $\boldsymbol{\gamma}_s$ instead of $\boldsymbol{\alpha}_s$ as the basic direction. In those cases the p.d.f. is in the form of $P\{\cos[\theta(\boldsymbol{\gamma}_{-\tau} - \boldsymbol{\gamma}_s)], \phi(\boldsymbol{\gamma}_{-\tau} - \boldsymbol{\beta}_s), \zeta(\boldsymbol{\alpha}_{-\tau} - \boldsymbol{\alpha}^P_s)\}$, involving a set of angles that start with the alignment of $\boldsymbol{\gamma}_{-\tau}$. Here, $\boldsymbol{\alpha}^P_s$ is the projection of $\boldsymbol{\alpha}_s$ onto the $(\boldsymbol{\beta}_{-\tau}, \boldsymbol{\alpha}_{-\tau})$-plane. Similarly, we use $P\{\cos[\theta(\boldsymbol{\alpha}_{-\tau} - \boldsymbol{\alpha}^{nl}_{-\tau})], \phi(\boldsymbol{\alpha}_{-\tau} - \boldsymbol{\beta}^{nl}_{-\tau}), \zeta(\boldsymbol{\gamma}_{-\tau} - \boldsymbol{\gamma}^{nl,P}_{-\tau})\}$ to study the alignment of τ^d_{ij} in a coordinate system defined by the eigenvectors of the nonlinear model, τ^{nl}_{ij} (instead of those of $\tilde{S}_{ij}$).

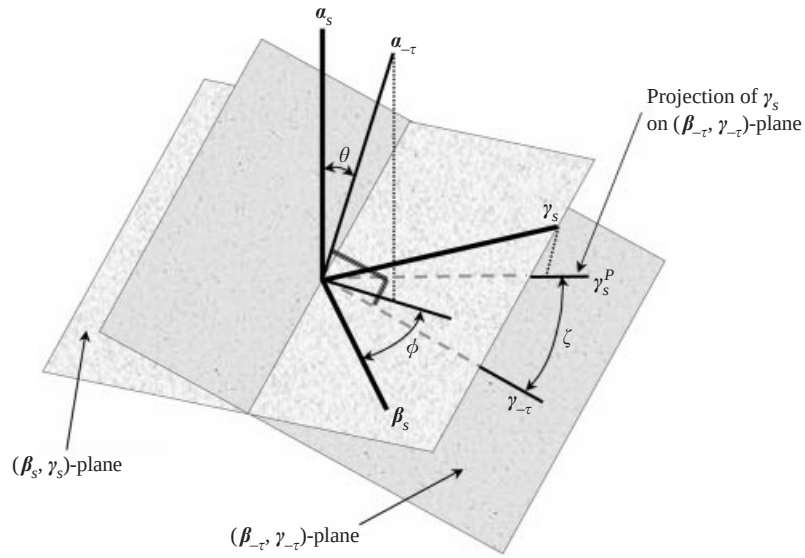

FIGURE 12. Definition of three angle variables for the three-dimensional joint p.d.f.s characterizing the alignment of an orthogonal tensor (say $-\tau_{ij}^d$) with another tensor (say $\tilde{S}_{ij}$). The angles are defined in terms of the tensor's respective eigenvectors.

4.2. *Alignment trends between* $\tilde{S}_{ij}$, τ_{ij}^d *and* τ_{ij}^{nl}

Figures 13(a) and 13(b) show the three-dimensional joint p.d.f. of relative alignment between $\tilde{S}_{ij}$ and $-\tau_{ij}^d$. The p.d.f. is computed by using $20 \times 20 \times 20$ bins of equal width for all three angle variables. For clarity, we present the alignment trends twice. Figure 13(a) shows the alignment of $\boldsymbol{\alpha}_{-\tau}$ better, whereas figure 13(b) illustrates the alignment of $\boldsymbol{\gamma}_{-\tau}$ more clearly. From figure 13(b), it is evident that $\boldsymbol{\gamma}_{-\tau}$ is preferentially aligned at 32° to $\boldsymbol{\gamma}_s$ (i.e. $\cos[\theta(\boldsymbol{\gamma}_{-\tau} - \boldsymbol{\gamma}_s)] \approx 0.85$) irrespective of the other angles. This trend is consistent with the results presented in Tao *et al.* (2000), but there the analysis was based on only two instantaneous realizations and the angle of preferred alignment was 34°. From figure 13(a) it is evident that there are actually two distinctive regions with high probability peaks. The first is located at $\cos[\theta(\boldsymbol{\alpha}_{-\tau} - \boldsymbol{\alpha}_s)] \approx 0.85$ (i.e. $\theta(\boldsymbol{\alpha}_{-\tau} - \boldsymbol{\alpha}_s) \approx 32°$), $\phi(\boldsymbol{\alpha}_{-\tau} - \boldsymbol{\beta}_s) \approx 90°$ and $\zeta(\boldsymbol{\gamma}_{-\tau} - \boldsymbol{\gamma}_s^P) \approx 0°$. The second peak is located at $\cos[\theta(\boldsymbol{\alpha}_{-\tau} - \boldsymbol{\alpha}_s)] \approx 0$ (i.e. $\theta(\boldsymbol{\alpha}_{-\tau} - \boldsymbol{\alpha}_s) \approx 90°$), $\phi(\boldsymbol{\alpha}_{-\tau} - \boldsymbol{\beta}_s) \approx 0°$ and $\zeta(\boldsymbol{\gamma}_{-\tau} - \boldsymbol{\gamma}_s^P) \approx 32°$. The first peak has only a very slightly higher value than the second one (~ 1.18 versus ~ 1.14). These two peaks indicate two preferred three-dimensional alignments, i.e. a bimodal behaviour. The alignments corresponding to the two p.d.f. peaks are illustrated by the two inserts in figure 13(a). The first peak corresponds to the $\alpha\beta\gamma$–$\alpha\beta\gamma$ configuration. Here, $\boldsymbol{\beta}_{-\tau}$ is parallel to $\boldsymbol{\beta}_s$, whereas $\boldsymbol{\alpha}_{-\tau}$ and $\boldsymbol{\gamma}_{-\tau}$ are located in the $(\boldsymbol{\alpha}_s, \boldsymbol{\gamma}_s)$-plane, each forming an angle of about 32° with its corresponding filtered strain-rate eigenvectors (i.e. $\boldsymbol{\alpha}_{-\tau}$ with $\boldsymbol{\alpha}_s$ and $\boldsymbol{\gamma}_{-\tau}$ with $\boldsymbol{\gamma}_s$). The second peak corresponds to the $\alpha\beta\gamma$–$\beta\alpha\gamma$ configuration. Here, $\boldsymbol{\alpha}_{-\tau}$ and $\boldsymbol{\beta}_{-\tau}$ switch places, i.e. $\boldsymbol{\alpha}_{-\tau}$ is now parallel to $\boldsymbol{\beta}_s$, whereas $\boldsymbol{\beta}_{-\tau}$ replaces $\boldsymbol{\alpha}_{-\tau}$ to form a 32° angle with $\boldsymbol{\alpha}_s$. Still, confirming the results in figure 13(b), $\boldsymbol{\gamma}_{-\tau}$ maintains the 32° angle with $\boldsymbol{\gamma}_s$.

In obtaining such results, we speculate whether the observed trends are due to a particular flow geometry of the present experimental facility. When the present analysis is performed using the DNS data of Cerutti & Meneveau (1998), the strong alignment trend of $\boldsymbol{\gamma}_{-\tau}$ and the bimodal behaviour of $\boldsymbol{\alpha}_{-\tau}$ still exist, as shown in

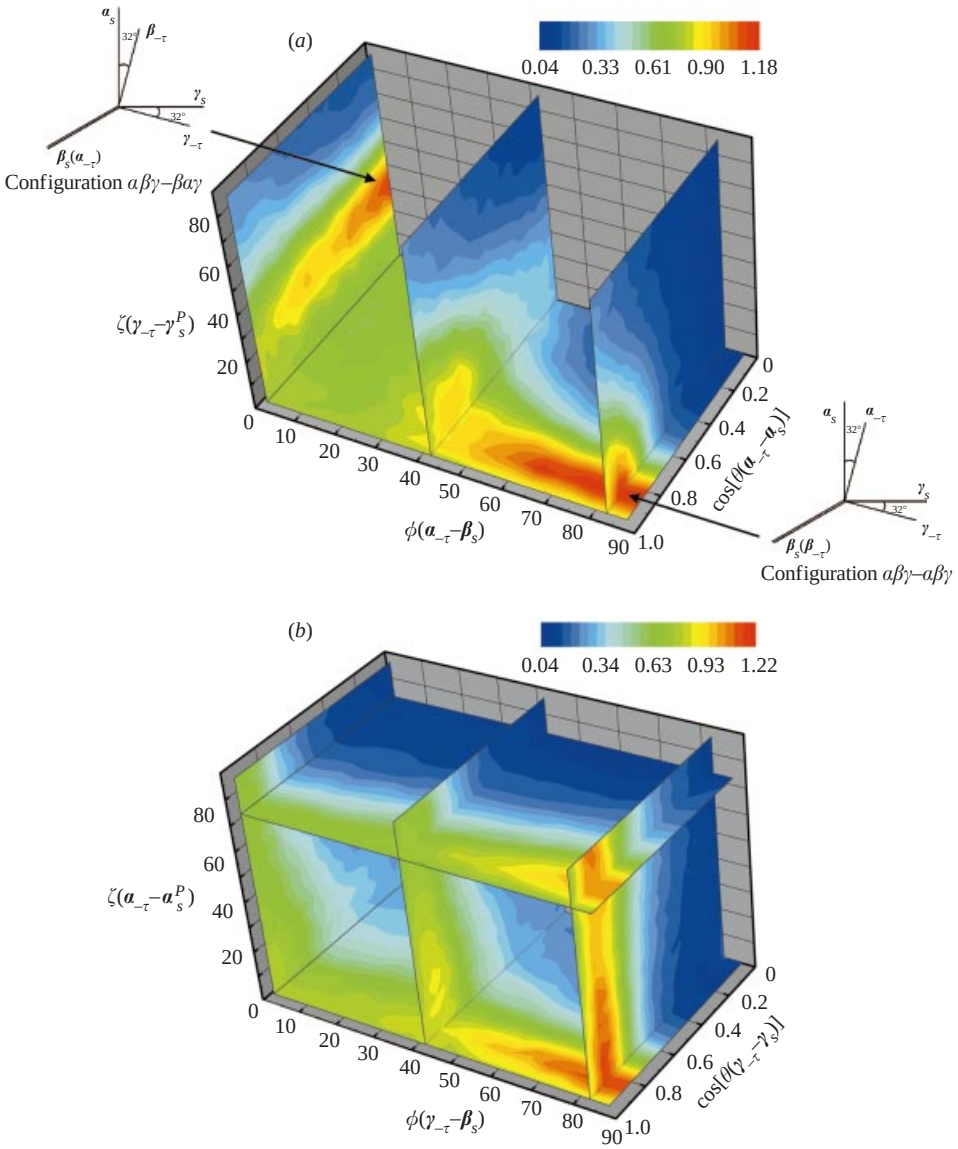

FIGURE 13. Joint p.d.f. of the relative alignment between eigenvectors of $\tilde{S}_{ij}$ and $-\tau_{ij}^d$: (*a*) $\boldsymbol{\alpha}_{-\tau}$ based, (*b*) $\boldsymbol{\gamma}_{-\tau}$ based. A random alignment with no discernible trends would correspond instead to a uniform probability density of $(\frac{1}{2}\pi)^{-2} \approx 0.396$.

figure 14. Thus, the presently observed trends are not unique to the current flow geometry. We will also show in § 5.4 that the bimodal behaviour of $\boldsymbol{\alpha}_{-\tau}$ is related to the magnitude of the vorticity (among other parameters). The configuration $\alpha\beta\gamma$–$\beta\alpha\gamma$ is much more pronounced in regions of high vorticity and the configuration $\alpha\beta\gamma$–$\alpha\beta\gamma$ becomes equally (or more) dominant in regions with intermediate levels of vorticity. Evidently, both configurations are not consistent with eddy viscosity models where it is assumed that the stress eigenvectors are aligned with the corresponding strain-rate eigenvectors.

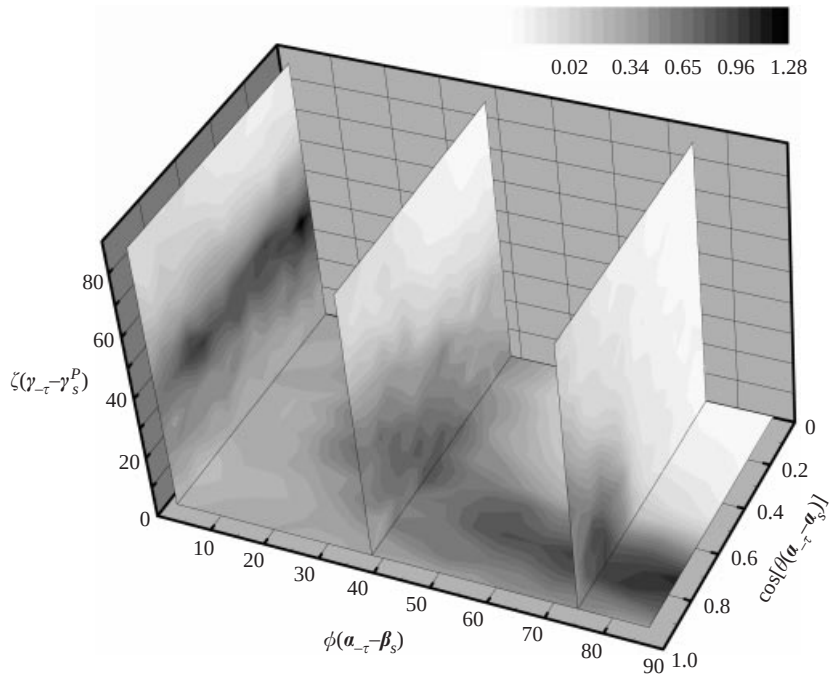

FIGURE 14. Probability density function of alignment between eigenvectors of $-\tau_{ij}^d$ and $\tilde{S}_{ij}$, evaluated from DNS results of isotropic turbulence at $Re_\lambda \approx 93$.

The alignment p.d.f. between the eigenvectors of τ_{ij}^d and τ_{ij}^{nl} is presented in figure 15. Here, the reference frame is defined by the eigenvectors of τ_{ij}^{nl}. The peak of $P\{\cos[\theta(\boldsymbol{\alpha}_{-\tau} - \boldsymbol{\alpha}_{-\tau}^{nl})], \phi(\boldsymbol{\alpha}_{-\tau} - \boldsymbol{\beta}_{-\tau}^{nl}), \zeta(\boldsymbol{\gamma}_{-\tau} - \boldsymbol{\gamma}_{-\tau}^{nl,P})\}$ is centred at $\theta(\boldsymbol{\alpha}_{-\tau} - \boldsymbol{\alpha}_{-\tau}^{nl}) \approx 0^\circ$, $\phi(\boldsymbol{\alpha}_{-\tau} - \boldsymbol{\beta}_{-\tau}^{nl}) \approx 0^\circ$, and $\zeta(\boldsymbol{\gamma}_{-\tau} - \boldsymbol{\gamma}_{-\tau}^{nl,P}) \approx 0^\circ$. This peak corresponds to a most probable alignment that $\boldsymbol{\alpha}_{-\tau}$ is parallel to $\boldsymbol{\alpha}_{-\tau}^{nl}$, $\boldsymbol{\beta}_{-\tau}$ is parallel to $\boldsymbol{\beta}_{-\tau}^{nl}$, and $\boldsymbol{\gamma}_{-\tau}$ is parallel to $\boldsymbol{\gamma}_{-\tau}^{nl}$. The magnitude of the peak probability is also three times as much as the results presented in figure 13. The nonlinear model evidently predicts the spatial orientations of the SGS stress eigenvectors much better than the eddy viscosity models. This conclusion is consistent with earlier findings in *a priori* tests (see Meneveau & Katz 2000) that were based on correlation coefficients (and were thus less easy to understand geometrically).

However, the p.d.f. peak in figure 15 is fairly broad with different ranges for each of the three angles. For $\theta(\boldsymbol{\alpha}_{-\tau} - \boldsymbol{\alpha}_{-\tau}^{nl}) \approx 0^\circ$, it seems that $\phi(\boldsymbol{\alpha}_{-\tau} - \boldsymbol{\beta}_{-\tau}^{nl})$ can have any value between 0° and 90°. To explain this result, note that when $\theta(\boldsymbol{\alpha}_{-\tau} - \boldsymbol{\alpha}_{-\tau}^{nl}) \approx 0^\circ$, the projection of $\boldsymbol{\alpha}_{-\tau}$ on the $\boldsymbol{\beta}_{-\tau}^{nl} - \boldsymbol{\gamma}_{-\tau}^{nl}$ plane is very small, and as a result small changes would generate a wide range of values for $\phi(\boldsymbol{\alpha}_{-\tau} - \boldsymbol{\beta}_{-\tau}^{nl})$. Furthermore, as is evident from figure 12, when $\phi(\boldsymbol{\alpha}_{-\tau} - \boldsymbol{\beta}_{-\tau}^{nl}) \approx 0^\circ$, $\boldsymbol{\gamma}_{-\tau}^{nl}$ is aligned with the intersection of the two planes, and $\zeta(\boldsymbol{\gamma}_{-\tau} - \boldsymbol{\gamma}_{-\tau}^{nl,P}) \approx 0^\circ$ implies that $\boldsymbol{\gamma}_{-\tau}$ is parallel to $\boldsymbol{\gamma}_{-\tau}^{nl}$. Under these conditions, the most likely $\theta(\boldsymbol{\alpha}_{-\tau} - \boldsymbol{\alpha}_{-\tau}^{nl})$ is 0°, but the probability remains high for a wide range of values of $\theta(\boldsymbol{\alpha}_{-\tau} - \boldsymbol{\alpha}_{-\tau}^{nl})$. This trend implies that there is a significant likelihood of $\boldsymbol{\alpha}_{-\tau}$ attaining any angle relative to $\boldsymbol{\beta}_{-\tau}^{nl}$ in the $(\boldsymbol{\alpha}_{-\tau}^{nl}, \boldsymbol{\beta}_{-\tau}^{nl})$-plane.

The alignment between the eigenvectors of $-\tau_{ij}^{nl}$ and $\tilde{S}_{ij}$, shown in figure 16, bears remarkable resemblance to the stress–strain alignment of figure 13(*a*). Here again,

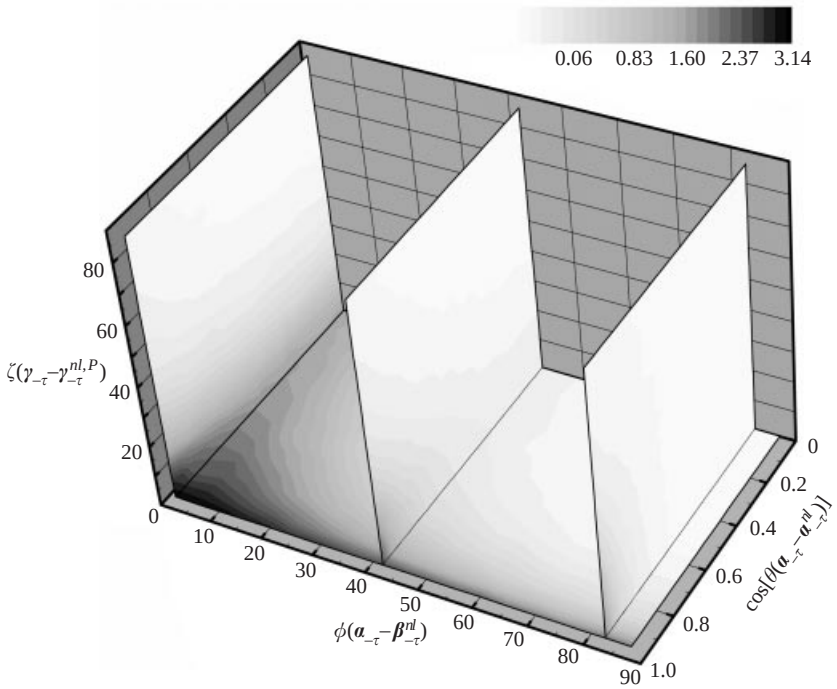

FIGURE 15. Probability density function of alignment between eigenvectors of τ_{ij}^{nl} and τ_{ij}^{d}.

a clearly defined bimodal behaviour exists, but the preferred alignment angles are around 42° instead of 32°. The implications of this difference in preferred alignment are discussed in § 6.4. Furthermore, the probability peak values are extremely high compared to those in figure 13(*a*), indicating an almost deterministic relative alignment. For example, the peak value corresponding to $\cos[\theta(\boldsymbol{\alpha}^{nl}_{-\tau} - \boldsymbol{\alpha}_s)] \approx 0.74$ ($\theta(\boldsymbol{\alpha}^{nl}_{-\tau} - \boldsymbol{\alpha}_s) \approx 42°$), $\phi(\boldsymbol{\alpha}^{nl}_{-\tau} - \boldsymbol{\beta}_s) \approx 90°$ and $\zeta(\boldsymbol{\gamma}^{nl}_{-\tau} - \boldsymbol{\gamma}^{P}_{s}) \approx 0°$ is around 8.3. This strong orientation is not entirely surprising, considering that both τ_{ij}^{nl} and $\tilde{S}_{ij}$ are constructed from common ingredients (elements of the filtered velocity gradient tensor).

5. Geometric alignment statistics conditioned on scalar flow parameters

Up to this point we have used all the data to investigate the relative alignment of SGS stress eigenvectors in frames of reference defined by the filtered strain-rate tensor and the eigenvectors of the nonlinear (similarity) model. In order to understand some of the observed trends, we perform a series of conditional samplings based on the magnitudes of SGS dissipation (§ 5.1), strain-rate (§ 5.2), stress and strain state parameters (§ 5.3), as well as the vorticity (§ 5.4). As will be demonstrated, the relative alignments are affected substantially by these parameters. While performing these conditional samplings we only use fractions of the data set. In evaluating the significance and/or impact of a specific condition, it is important to know what percentage of the flow field satisfies that condition. These conditions and associated data percentages are presented in table 1.

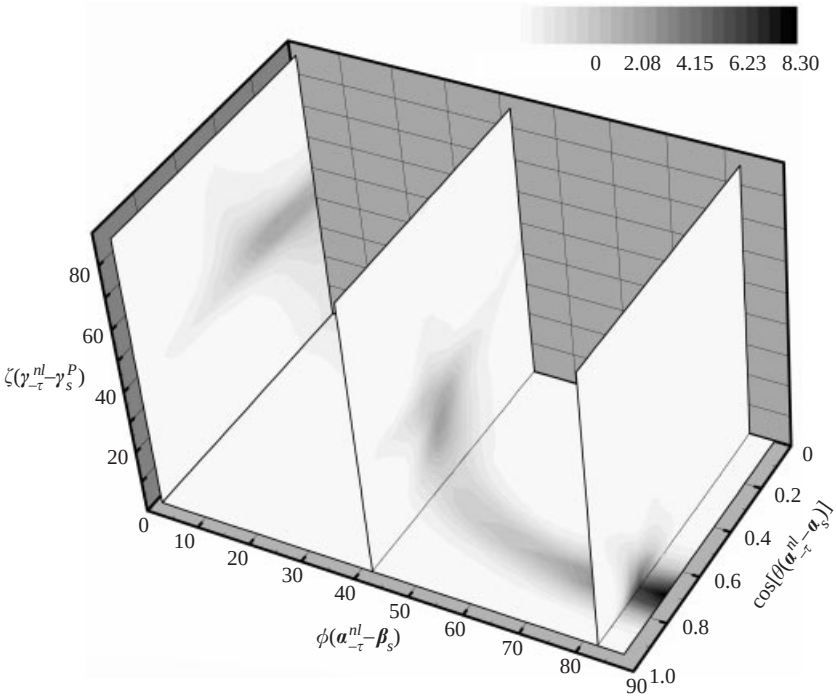

FIGURE 16. Probability density function of alignment between eigenvectors of $-\tau^{nl}_{ij}$ and $\tilde{S}_{ij}$.

Variables	Conditional sampling ranges and sample sizes				
Π/Π_{mean}	$-\infty \to -1$	$-1 \to 0$	$0 \to 1$	$1 \to 4$	$4 \to \infty$
	2.8%	21.0%	45.2%	24.9%	6.1%
s^*	$-1 \to 0$	$0 \to 0.6$	$0.6 \to 0.9$	$0.9 \to 1$	
	32.4%	31.7%	25.0%	10.9%	
s^*_τ	$-1 \to -0.95$	$-0.95 \to -0.6$	$-0.6 \to 0$	$0 \to 1$	
	10.6%	37.5%	28.4%	23.5%	
$\lvert\tilde{\mathbf{s}}\rvert/\sigma_{\lvert\tilde{\mathbf{s}}\rvert}$	$0 \to 2$	$2 \to 4$	$4 \to \infty$		
	39.6%	53.3%	7.1%		
$\lvert\tilde{\boldsymbol{\omega}}\rvert/\sigma_{\lvert\tilde{\omega}\rvert}$	$0 \to 1.5$	$1.5 \to 4$	$4 \to \infty$		
	36.8%	59.3%	3.9%		

TABLE 1. Selected conditions and percentages of the data set used in the conditional sampling. The upper row indicates a condition (or range) and the lower row shows the percentage.

5.1. *Conditional sampling based on SGS dissipation*

Results of conditional sampling based on the value of SGS dissipation are presented in figure 17. The bimodal behaviour that is observed while examining the entire data set (§4.2) is still present in all the conditional p.d.f.s. However, both angles of peak probability increase from about 28° when $\Pi/\Pi_{mean} \geqslant 4$ (figure 17*a*) to 36° when $0 \leqslant \Pi/\Pi_{mean} < 1$ (figure 17*b*) and to about 55° when $\Pi/\Pi_{mean} < -1$ (figure 17*c*). The magnitudes of the peaks in regions of both high positive and high negative dissipation are much higher than those of the entire data, indicating stronger alignment trends. In regions of low positive dissipation (figure 17*b*), the p.d.f. has broader peaks with lower magnitudes, but not as low as the p.d.f. peaks of the entire dataset. For all

cases, the illustrations of preferred alignment (figure 13*a*) still apply, but with different angles, i.e. 28°, 36° and 55° replacing the 32° for the conditions shown in figures 17(*a*) to 17(*c*), respectively. These angular variations are to be expected since negative SGS dissipation occurs when $\boldsymbol{\gamma}_{-\tau}$ approaches $\boldsymbol{\alpha}_s$, and $\boldsymbol{\alpha}_{-\tau}$ (or $\boldsymbol{\beta}_{-\tau}$) approaches $\boldsymbol{\gamma}_s$. Finally, note that in regions of high negative dissipation, the peak corresponding to $\phi(\boldsymbol{\alpha}_{-\tau} - \boldsymbol{\beta}_s) \approx 0°$ is significantly higher than the peak at $\phi(\boldsymbol{\alpha}_{-\tau} - \boldsymbol{\beta}_s) \approx 90°$. Thus, the alignment of configuration $\alpha\beta\gamma$–$\beta\alpha\gamma$, with an angle of 55°, is more dominant. However, as table 1 shows, this condition is quite infrequent (2.8% of the time).

The effects of Π on the relative alignment between $-\tau_{ij}^d$ and τ_{ij}^{nl} are less complicated. The strong alignment of $\boldsymbol{\gamma}_{-\tau}$ with $\boldsymbol{\gamma}_{-\tau}^{nl}$ and the clear but weaker alignment of $\boldsymbol{\alpha}_{-\tau}$ with $\boldsymbol{\alpha}_{-\tau}^{nl}$ persist in all the conditional p.d.f.s (results not shown). The peak values in regions of high positive dissipation are much higher than those of the unconditional case. These peaks are lower and less concentrated in lower dissipation ranges, but the trends remain unchanged.

5.2. *Conditional sampling based on strain-rate magnitude*

Figure 18 shows the effect of $|\tilde{\boldsymbol{S}}|$ on the alignment trends of $-\tau_{ij}^d$ eigenvectors relative to those of $\tilde{S}_{ij}$. In regions of high $|\tilde{\boldsymbol{S}}|$ (figure 18*a*), the locations of the two peaks at offset angles of 32° remain unchanged. However, the magnitudes of both peaks increase substantially (from 1.2 to 2.9) and they appear to be more concentrated. In regions of intermediate strain-rate (figure 18*b*) the peaks have a significantly broader extent, and their magnitudes decrease to a level that is only slightly higher than that of the entire data (compared to figure 13). Conversely, in regions of low $|\tilde{\boldsymbol{S}}|$, as shown in figure 18(*c*), the alignment trends are noticeably different. The preferred alignments sketched in figure 14 no longer exist, and the probability peaks instead shift to $\theta(\boldsymbol{\alpha}_{-\tau} - \boldsymbol{\alpha}_s) \approx 0°$. However, the peaks become very broad with fairly low magnitudes. To recapitulate, in highly strained regions the most extensive and most contracting SGS stresses (or intermediate stress when $\boldsymbol{\beta}_{-\tau}$ and $\boldsymbol{\alpha}_{-\tau}$ switch places) are 'forced' to form an angle of 32° with the corresponding eigenvectors of the strain-rate. As the strain-rate magnitude decreases the SGS stress eigenvectors shift towards their respective strain-rate counterparts (as in eddy-viscosity), but the probability peaks broaden and their magnitudes decrease.

Conditional sampling of the alignment relative to τ_{ij}^{nl} based on $|\tilde{\boldsymbol{S}}|$ does not show substantial variations in trends. As a result, they are not shown. The strong alignment of $\boldsymbol{\gamma}_{-\tau}$ with $\boldsymbol{\gamma}_{-\tau}^{nl}$ persists and so is the broader range for the alignment of $\boldsymbol{\alpha}_{-\tau}$ with $\boldsymbol{\alpha}_{-\tau}^{nl}$ (see figure 15). The only effect of decreasing $|\tilde{\boldsymbol{S}}|$ is a reduction in peak probability. For example, the peak values for $|\tilde{\boldsymbol{S}}|/\sigma_{|\tilde{\boldsymbol{S}}|} \geqslant 4$, $2 \leqslant |\tilde{\boldsymbol{S}}|/\sigma_{|\tilde{\boldsymbol{S}}|} < 4$, and $|\tilde{\boldsymbol{S}}|/\sigma_{|\tilde{\boldsymbol{S}}|} < 2$ are 10, 3.4 and 1.6, respectively. Thus, for all cases these peaks are considerably higher than those with the $\tilde{S}_{ij}$ eigenvectors.

5.3. *Conditional sampling based on s_τ^* and s^**

The effects of the SGS stress state, characterized by s_τ^*, on the alignment trends are shown in figure 19. In regions of near axisymmetric contraction ($-1 \leqslant s_\tau^* < -0.95$, figure 19*a*), the bimodal alignment is evident, with probability peaks that are almost twice as high as those of the entire data. The preferred $\theta(\boldsymbol{\alpha}_{-\tau} - \boldsymbol{\alpha}_s)$ when $\phi(\boldsymbol{\alpha}_{-\tau} - \boldsymbol{\beta}_s) \approx 90°$ is about 35°, slightly greater than that of the entire dataset. The preferred $\zeta(\boldsymbol{\gamma}_{-\tau} - \boldsymbol{\gamma}_s^P)$ (which for $\phi(\boldsymbol{\alpha}_{-\tau} - \boldsymbol{\beta}_s) \approx 0°$ is also equal to $\theta(\boldsymbol{\gamma}_{-\tau} - \boldsymbol{\gamma}_s)$) is about 37°, also greater than the results in figure 13. As s_τ^* increases, both $\theta(\boldsymbol{\alpha}_{-\tau} - \boldsymbol{\alpha}_s)$ and $\zeta(\boldsymbol{\gamma}_{-\tau} - \boldsymbol{\gamma}_s^P)$ at the points of maximum probability decrease. In the $-0.95 \leqslant s_\tau^* < -0.6$ range (37.5% of the data), the most probable angles are $\theta(\boldsymbol{\alpha}_{-\tau} - \boldsymbol{\alpha}_s) \approx 35°$ and

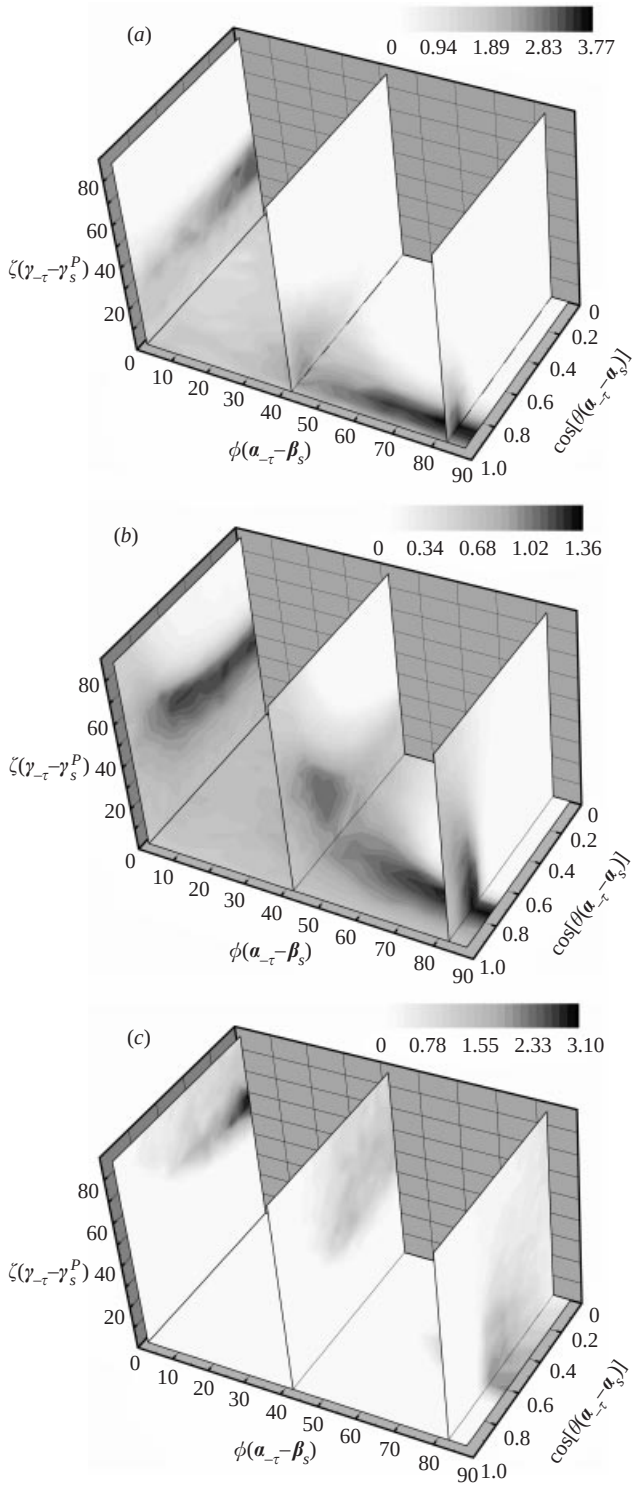

FIGURE 17. Conditional joint p.d.f.s based on SGS dissipation: (*a*) $\Pi/\Pi_{mean} \geqslant 4$, (*b*) $0 \leqslant \Pi/\Pi_{mean} < 1$, (*c*) $\Pi/\Pi_{mean} < -1$.

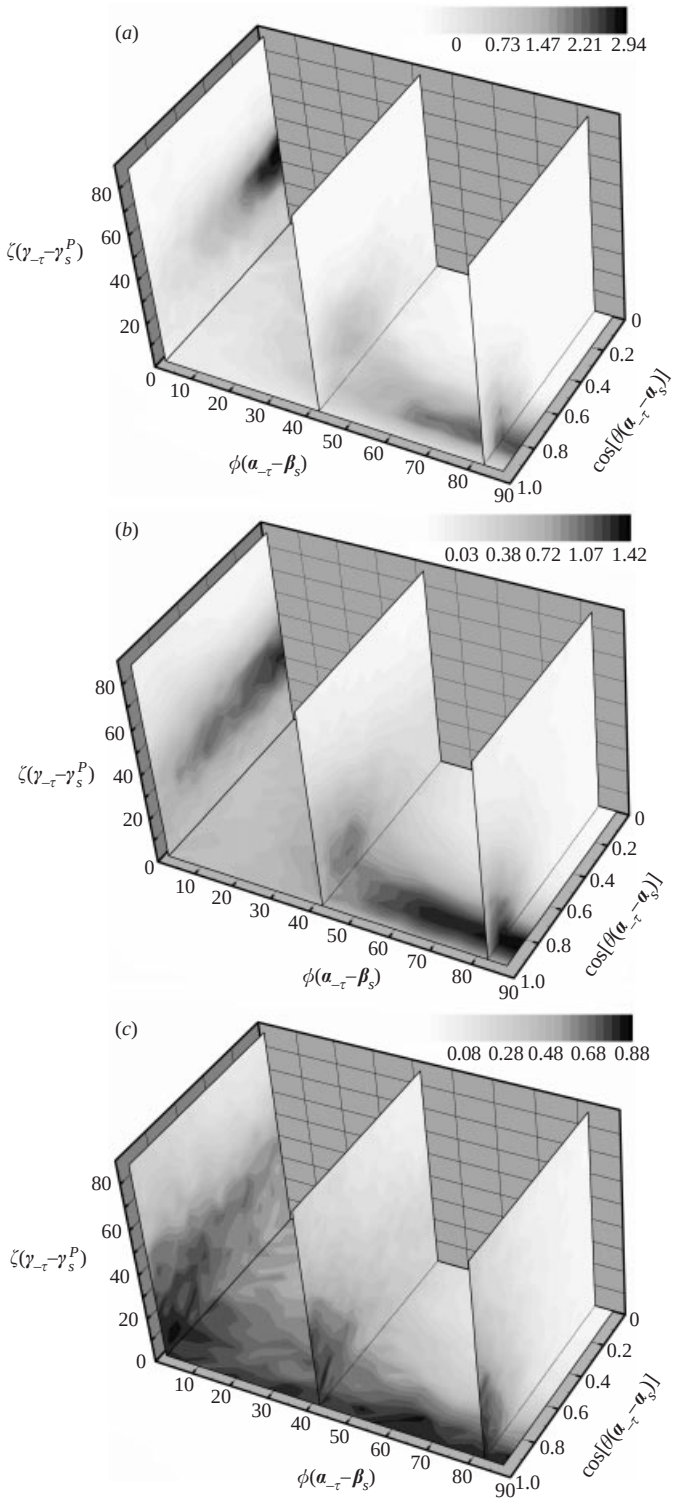

FIGURE 18. Conditional joint p.d.f.s based on strain-rate magnitude: (*a*) $|\tilde{\mathbf{S}}|/\sigma_{|\tilde{\mathbf{S}}|} \geqslant 4$, (*b*) $2 \leqslant |\tilde{\mathbf{S}}|/\sigma_{|\tilde{\mathbf{S}}|} < 4$, (*c*) $|\tilde{\mathbf{S}}|/\sigma_{|\tilde{\mathbf{S}}|} < 2$.

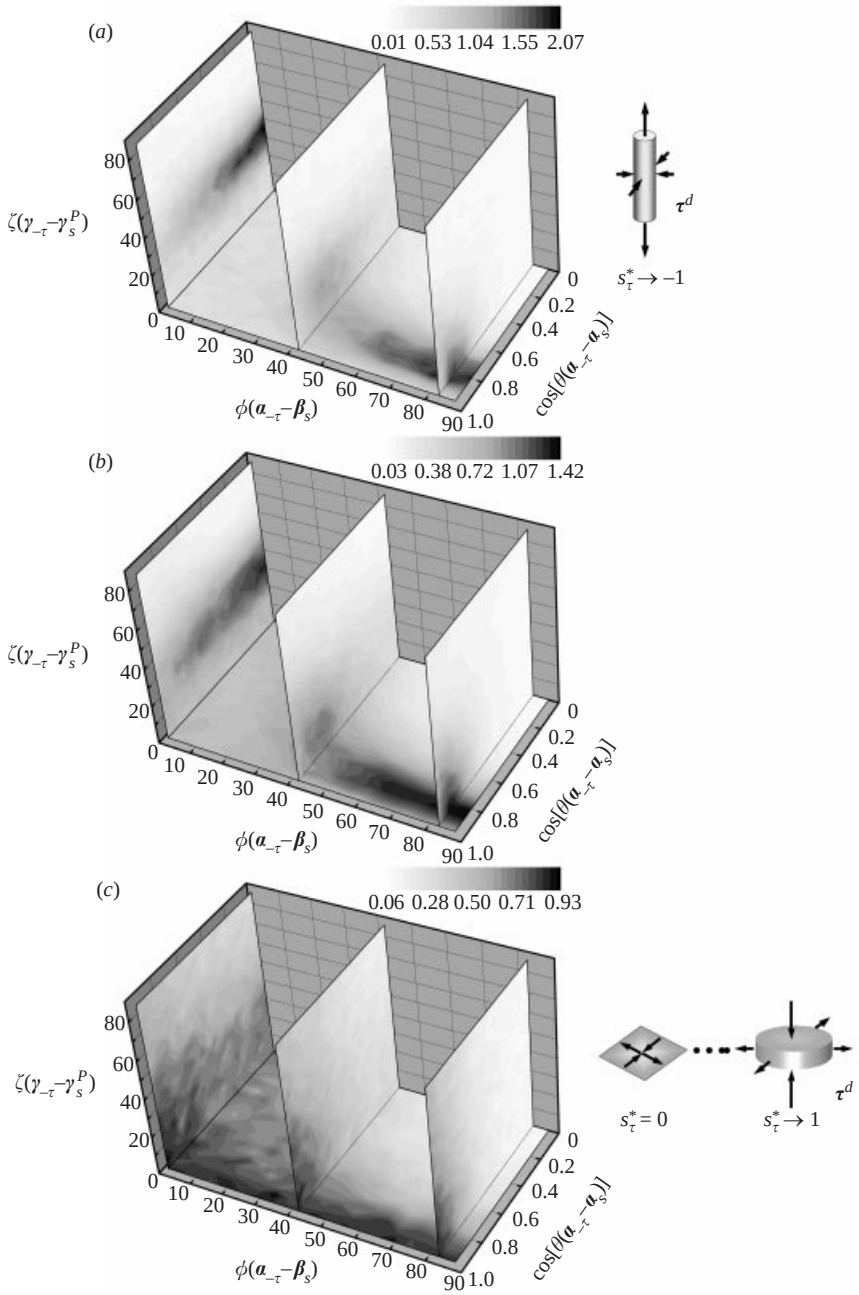

FIGURE 19. Conditional joint p.d.f.s based on s_τ^*: (*a*) $-1 \leqslant s_\tau^* < -0.95$, (*b*) $-0.95 \leqslant s_\tau^* < -0.6$, (*c*) $s_\tau^* \geqslant 0$. The illustrations in (*a*) and (*c*) demonstrate the configuration/structure of the stress eigenvalues for the corresponding values of s_τ^*.

$\zeta(\gamma_{-\tau} - \gamma_s^P) \approx 32^\circ$. The magnitudes of both p.d.f. peaks also decrease and the domain connecting the two peaks has an increasingly higher probability. This trend continues with increasing s_τ^*, and the peaks become broader and extend with small variations towards $\theta(\alpha_{-\tau} - \alpha_s) \approx 0^\circ$. Especially when $s_\tau^* > 0$ (figure 19*c*), which accounts for

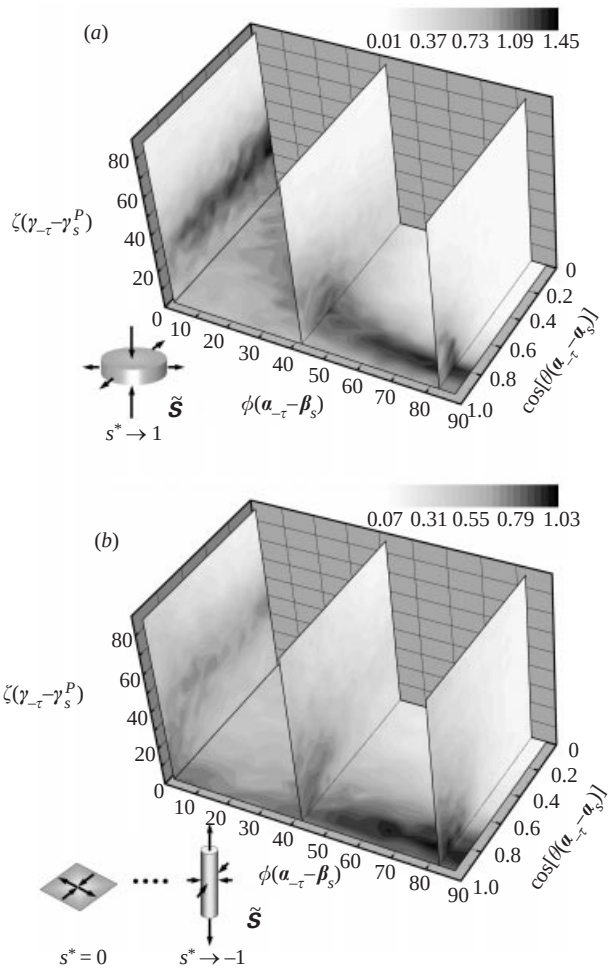

FIGURE 20. Conditional joint p.d.f.s based on s^*: (*a*) $0.9 \leqslant s^* \leqslant 1$, (*b*) $s^* < 0$. The illustrations show the structure of the filtered strain-rate eigenvectors for the corresponding values of s^* (The same illustration of (*b*) also appears in figure 27*b*.)

23.5% of the data, there is a clear shift in the location of the peak to $\theta(\boldsymbol{\alpha}_{-\tau} - \boldsymbol{\alpha}_s) \approx 0^\circ$, and the peak magnitude also decreases. The second peak essentially disappears and the preferred value of $\zeta(\boldsymbol{\gamma}_{-\tau} - \boldsymbol{\gamma}_s^P)$, even though within a fairly broad range, also decreases to zero. Thus, there is a clear trend of shifting alignment as s_τ^* changes.

Unlike the substantial changes in alignment that occur with varying s_τ^*, varying s^* seems to have less impact on the preferred orientation of τ_{ij}^d. Consequently, only two samples of extreme conditions are presented in figures 20(*a*) and 20(*b*). The probability peaks remain small, varying between 1.03 and 1.45 as s^* increases from negative values to the high positive range and the bimodal trend persists for all values of s^*. The preferred orientation corresponding to $\phi(\boldsymbol{\alpha}_{-\tau} - \boldsymbol{\beta}_s) \approx 90^\circ$ (configuration $\alpha\beta\gamma$–$\alpha\beta\gamma$) remains $\theta(\boldsymbol{\alpha}_{-\tau} - \boldsymbol{\alpha}_s) \approx 32^\circ$. The preferred angle of the second probability peak, i.e. at $\phi(\boldsymbol{\alpha}_{-\tau} - \boldsymbol{\beta}_s) \approx 0^\circ$ (corresponding to configuration $\alpha\beta\gamma$–$\beta\alpha\gamma$) increases as s^* decreases. When $0.9 \leqslant s^* \leqslant 1$, it is $\zeta(\boldsymbol{\gamma}_{-\tau} - \boldsymbol{\gamma}_s^P) \approx 25^\circ$ but the peak is broad and extends almost to 40°. Conversely, in regions of negative s^*, as illustrated in figure 20(*b*), the trend is reversed and the peak at $\phi(\boldsymbol{\alpha}_{-\tau} - \boldsymbol{\beta}_s) = 90^\circ$ becomes clearly

dominant. Of all the conditional samplings, $s^* < 0$ is the most obvious case where the peak corresponding to configuration $\alpha\beta\gamma$–$\alpha\beta\gamma$ remains and the second peak almost disappears (there are cases where they both disappear). Clearly, and consistent with the discussions in § 3.1, the difference in trends between s^*_τ and s^* indicate again that they are decoupled.

The effect of s^*_τ on the relative alignment between the eigenvectors of τ^d_{ij} and τ^{nl}_{ij} is even less significant (data not shown). The preferred alignment remains unchanged and quite similar to the result shown in figure 15. However, the magnitude of the probability peak decreases with increasing s^*_τ. Conditional sampling based on s^* of the alignment relative to τ^{nl}_{ij} (not shown) also does not show significant differences in trends, except for a decrease in peak probability when s^* is negative.

5.4. *Filtered vorticity vector: its alignment and effects on SGS stress alignments*

5.4.1. *Alignment trends of filtered vorticity vector*

As noted in § 1.2, previous numerical and experimental studies and our own results indicate that the vorticity is preferentially aligned with the intermediate $\tilde{S}_{ij}$ eigenvector ($\boldsymbol{\beta}_s$). In Tao *et al.* (2000), we also show (using only two instantaneous distributions) that $\tilde{\omega}_i$ is preferentially located in a plane perpendicular to the most extensive eigenvector of $\tau^d_{ij}(\boldsymbol{\gamma}_{-\tau})$. The analysis is repeated using nine vector maps and the results are presented in figures 21 and 22. Each plot is a two-dimensional joint p.d.f. showing the preferred alignment of the vorticity vector. Figure 21(*a*) shows the alignment in a frame of reference defined by the eigenvectors of $\tilde{S}_{ij}$, and figures 21(*b*) and 22(*a–c*) display the alignments in the eigenframe of $-\tau^d_{ij}$.

The preferred alignment of $\tilde{\omega}_i$ with $\boldsymbol{\beta}_s$ is evident in figure 21(*a*). Conditional sampling based on $|\tilde{\mathbf{S}}|$, Π and $|\tilde{\boldsymbol{\omega}}|$ does not change this trend (results not shown), but the peak probability at the same angle increases with increasing magnitude of any of these parameters. Conditional sampling based on the magnitude of s^*_τ (also not shown) does not affect the preferred angle, but the peak probability decreases slightly with increasing s^*_τ. The only parameter that has some effect on the alignment of $\tilde{\omega}_i$ relative to the $\tilde{S}_{ij}$ eigenvectors is s^*. In regions of $s^* \to 1$, α_s and β_s have comparable magnitudes and therefore they cannot be distinguished from each other. As a result the iso-probability lines at $\cos[\theta(\boldsymbol{\omega} - \boldsymbol{\gamma}_s)] \to 0$ become more and more parallel to the ϕ axis (data not shown). Thus, as $s^* \to 1$, $\tilde{\omega}_i$ is equally likely to be aligned anywhere in the $(\boldsymbol{\alpha}_s, \boldsymbol{\beta}_s)$-plane. Finally, since β_s can be either positive or negative (see figure 5*c*), it is also of interest to examine whether the p.d.f. changes owing to stretching or contraction. Although the location of the peak does not change, the probability does. In regions with stretching ($\beta_s > 0$) the p.d.f. peaks (not shown) are considerably higher than those in regions with contraction. $\beta_s < 0$ also causes another interesting effect – it substantially reduces the likelihood that the vorticity is aligned with $\boldsymbol{\alpha}_s$.

In the SGS stress reference frame (figure 21*b*), the vorticity is preferentially aligned with $\alpha_{-\tau}$. However, the probability gradients with varying $\phi(\boldsymbol{\omega} - \boldsymbol{\beta}_{-\tau})$ are quite small, i.e. a considerable fraction of the vorticity is aligned at other angles in the $(\boldsymbol{\alpha}_{-\tau}, \boldsymbol{\beta}_{-\tau})$-plane. The results also indicate that $\tilde{\omega}_i$ is preferentially perpendicular to $\boldsymbol{\gamma}_{-\tau}$. In Tao *et al.* 2000, where the results are based on only two instantaneous distributions, we have also concluded that $\tilde{\omega}_i$ is perpendicular to $\boldsymbol{\gamma}_{-\tau}$, but the preferred alignment with $\boldsymbol{\alpha}_{-\tau}$ compared to that with $\boldsymbol{\beta}_{-\tau}$ is weak (peaks of 1.04 and 0.95 at $\boldsymbol{\alpha}_{-\tau}$ and $\boldsymbol{\beta}_{-\tau}$, respectively). As we have obtained more data, the p.d.f. peaks have shifted to the present values, 1.2 and 0.85, respectively.

Conditional sampling based on Π or $|\tilde{\mathbf{S}}|$ (not shown) does not change the preferred alignment angles. With increasing Π or $|\tilde{\mathbf{S}}|$, the probability peak shifts further towards

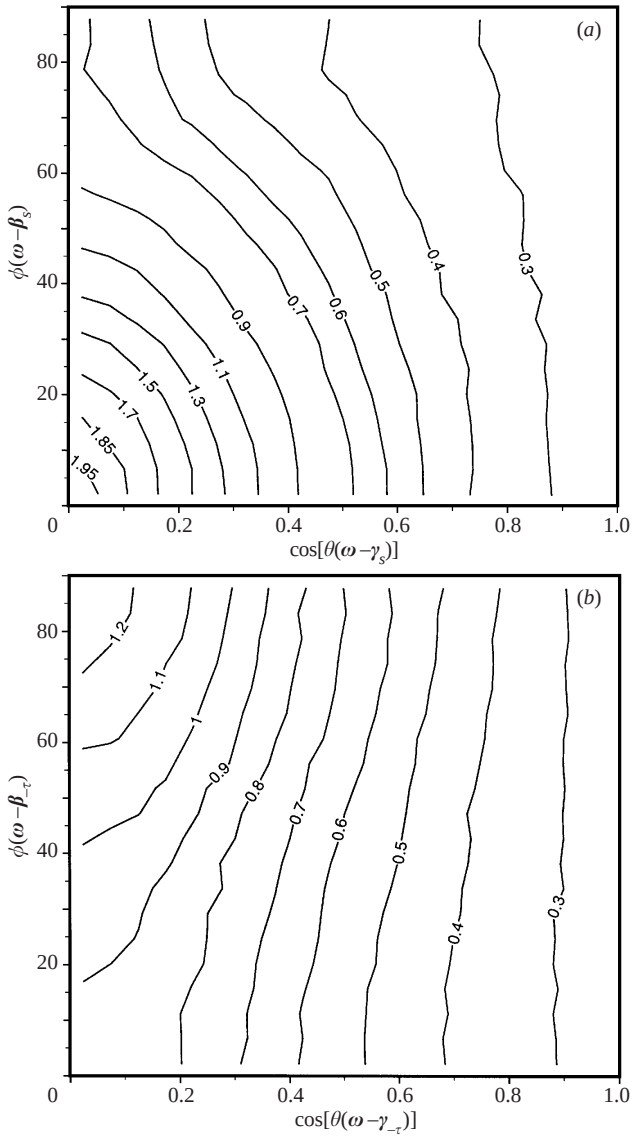

FIGURE 21. Joint p.d.f. of relative alignment between $\tilde{\boldsymbol{\omega}}$ and eigenvectors of (*a*) $\tilde{S}_{ij}$, (*b*) $-\tau^d_{ij}$.

$\cos[\theta(\boldsymbol{\omega}-\boldsymbol{\gamma}_{-\tau})] = 0$ and the bias towards $\boldsymbol{\alpha}_{-\tau}$ compared to $\boldsymbol{\beta}_{-\tau}$ remains, but to a lesser extent. Conditional sampling based on the magnitude of s^* (not shown) affects only the magnitude of peaks. Conditional sampling based on s^*_τ shows significant changes only for $-1 \leqslant s^*_\tau < -0.95$, when the SGS stresses are essentially axisymmetric and the difference between $\boldsymbol{\alpha}_{-\tau}$ and $\boldsymbol{\beta}_{-\tau}$ diminishes. Consequently, $\tilde{\omega}_i$ can be aligned with almost the same probability at any angle in the $(\boldsymbol{\alpha}_{-\tau}, \boldsymbol{\beta}_{-\tau})$-plane. For higher values of s^*_τ the p.d.f.s are quite similar to figure 21(*b*) with only a small decrease in the peak probability as s^*_τ increases.

Substantial changes in alignment occur when the data are conditionally sampled based on $|\tilde{\boldsymbol{\omega}}|$, as shown in figure 22. In regions of high $|\tilde{\boldsymbol{\omega}}|$ (figure 22*a*) the vorticity is strongly aligned with $\boldsymbol{\alpha}_{-\tau}$. When the p.d.f. is further conditioned on $\beta_s > 0$ (relying

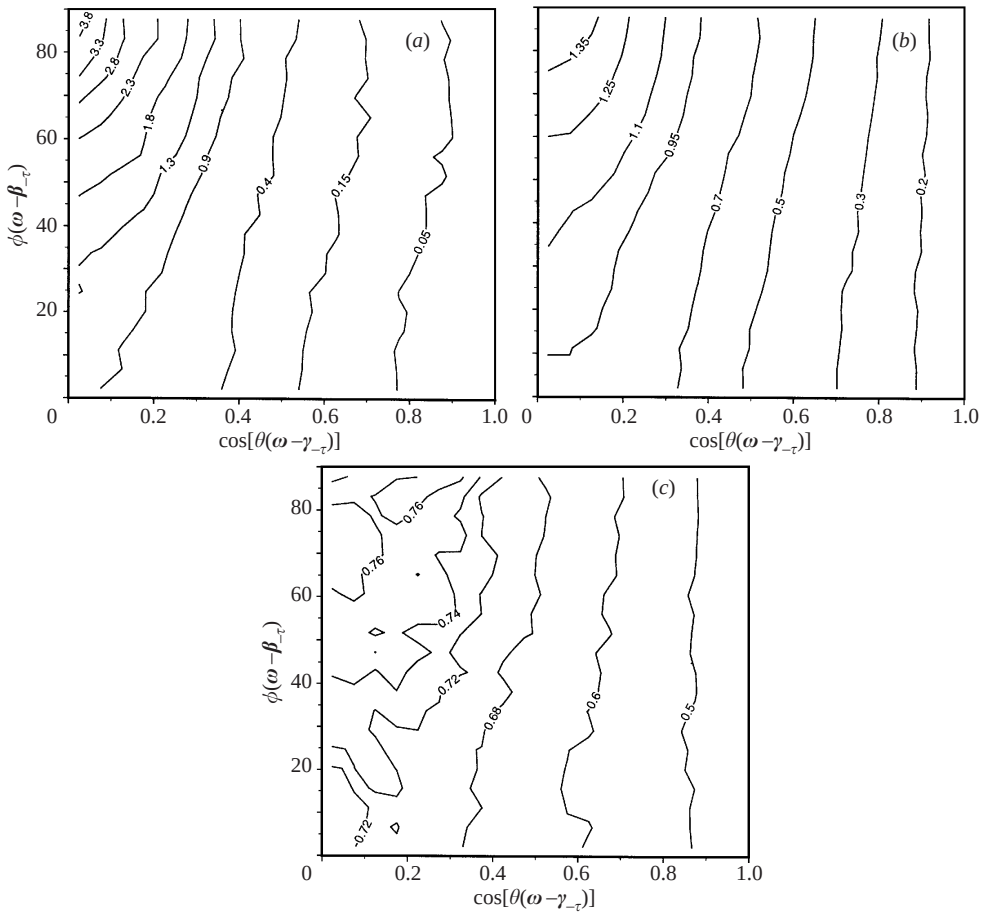

FIGURE 22. Conditional p.d.f.s of alignment between $\tilde{\omega}$ and eigenvectors of $-\tau_{ij}^d$, based on the vorticity magnitude: (*a*) $|\tilde{\omega}|/\sigma_{|\tilde{\omega}|} \geqslant 4$, (*b*) $1.5 \leqslant |\tilde{\omega}|/\sigma_{|\tilde{\omega}|} < 4$, (*c*) $|\tilde{\omega}|/\sigma_{|\tilde{\omega}|} < 1.5$.

on the fact that $\tilde{\omega}_i$ is aligned with $\boldsymbol{\beta}_s$), the probability peak increases slightly (to 4.3) and when conditioned on $\beta_s < 0$ it decreases (to 2.8). In regions of intermediate vorticity (figure 22*b*), the magnitude of the peak at $\boldsymbol{\alpha}_{-\tau}$ is considerably reduced, whereas the probability of being parallel to $\boldsymbol{\beta}_{-\tau}(\phi(\boldsymbol{\omega} - \boldsymbol{\beta}_{-\tau}) = 0^\circ)$ remains at almost the same level. Vortex stretching ($\beta_s > 0$) increases this peak at $\phi(\boldsymbol{\omega} - \boldsymbol{\beta}_{-\tau}) = 90^\circ$ slightly (to 1.4) and compression ($\beta_s < 0$) decreases it (to 1.3). In regions of low vorticity (figure 22*c*), the entire p.d.f. becomes increasingly uniform with only a slight preference to the $(\boldsymbol{\alpha}_{-\tau}, \boldsymbol{\beta}_{-\tau})$-plane. Clearly, with increasing magnitude, the vorticity is much more likely to be aligned with the most contracting stress eigenvector. As will be shown shortly, this trend also affects the relative alignment between $-\tau_{ij}^d$ and $\tilde{S}_{ij}$.

5.4.2. *Effects of filtered vorticity on SGS stress alignment trends*

The joint p.d.f. of three angles characterizing τ_{ij}^d alignments are recomputed using conditional sampling based on three ranges of vorticity magnitude. In regions of high vorticity ($|\tilde{\omega}|/\sigma_{|\tilde{\omega}|} \geqslant 4$), as shown in figure 23(*a*), there is a clear preference for one particular alignment configuration, $\theta(\boldsymbol{\alpha}_{-\tau} - \boldsymbol{\alpha}_s) \approx 90^\circ$, $\phi(\boldsymbol{\alpha}_{-\tau} - \boldsymbol{\beta}_s) \approx 0^\circ$,

$\zeta(\boldsymbol{\gamma}_{-\tau} - \boldsymbol{\gamma}_s^P) \approx 38^\circ$. This p.d.f. peak corresponds to the $\alpha\beta\gamma$–$\beta\alpha\gamma$ configuration with $\boldsymbol{\alpha}_{-\tau}$ aligned with $\boldsymbol{\beta}_{-\tau}$, except that the angles between $\boldsymbol{\gamma}_{-\tau}$ and $\boldsymbol{\gamma}_s$ as well as between $\boldsymbol{\beta}_{-\tau}$ and $\boldsymbol{\alpha}_s$ are now about 38°. When these high-vorticity regions are further divided to cases with positive and negative values of β_s (not shown), the trends differ. When $\beta_s > 0$, the peak at $\phi(\boldsymbol{\alpha}_{-\tau} - \boldsymbol{\beta}_s) \approx 0^\circ$ increases (to 3.9) and the second peak becomes more 'faded'. When $\beta_s < 0$, the peak at $\phi(\boldsymbol{\alpha}_{-\tau} - \boldsymbol{\beta}_s) \approx 0^\circ$ decreases (to 3.0) and shrinks to a smaller size ($\theta(\boldsymbol{\alpha}_{-\tau} - \boldsymbol{\alpha}_s) < 10^\circ$), whereas the second peak becomes more distinct. These results and the fact that in regions with high $|\tilde{\boldsymbol{\omega}}|$, the vorticity is strongly aligned with $\boldsymbol{\beta}_s$ and with $\boldsymbol{\alpha}_{-\tau}$, seem to indicate that the most contracting stress is preferentially aligned to oppose the stretching (by $\boldsymbol{\beta}_s$) of strong vortices. Of all the conditional samplings of the τ_{ij}^d–$\tilde{S}_{ij}$ alignment, this is the only case where the $\alpha\beta\gamma$–$\beta\alpha\gamma$ configuration is clearly dominant (excluding regions with high negative dissipation, where the angles are different).

In regions of intermediate vorticity, the bimodal behaviour returns with much lower probability peaks (figure 23*b*). The second preferred configuration, $\alpha\beta\gamma$–$\alpha\beta\gamma$, now has a slightly higher peak and both angles decrease to 32°. When this intermediate vorticity range is further divided to cases with positive and negative intermediate strain-rate (not shown), for $\beta_s > 0$ the peak at $\phi(\boldsymbol{\alpha}_{-\tau} - \boldsymbol{\beta}_s) \approx 0^\circ$ increases slightly and becomes larger than the peak at $\phi(\boldsymbol{\alpha}_{-\tau} - \boldsymbol{\beta}_s) \approx 90^\circ$ that decreases slightly. When $\beta_s < 0$ the peak at $\phi(\boldsymbol{\alpha}_{-\tau} - \boldsymbol{\beta}_s) \approx 0^\circ$ essentially disappears and the magnitude of the second peak also decreases (to 1.29). These trends lend further support to our claim that in regions where the vorticity is stretched by the intermediate strain, the most contracting stress eigenvector is preferentially aligned to oppose the vortex stretching. A plausible explanation for this trend is provided in § 6.4.

In regions with low vorticity (figure 23*c*), both p.d.f. peaks disappear, and the preferred alignment, with low and broad probability peaks, shifts to $\theta(\boldsymbol{\alpha}_{-\tau} - \boldsymbol{\alpha}_s) \approx 0^\circ$. Thus, the trends at low vorticity are essentially the same as those at low strain-rate magnitude. To illustrate that these results are not only characteristic to the present geometry, we repeat the conditional sampling using the isotropic turbulence data of Cerutti & Meneveau (1998). Similar trends are observed for the case of $|\tilde{\boldsymbol{\omega}}|/\sigma_{|\tilde{\boldsymbol{\omega}}|} \geqslant 4$ (data not shown).

Like all the other parameters, the effect of $|\tilde{\boldsymbol{\omega}}|$ on the alignment of τ_{ij}^d with τ_{ij}^{nl} is much less significant (data not shown). The preferred alignment remains unchanged and similar to figure 15. However, the magnitude of the probability peak increases rapidly with increasing $|\tilde{\boldsymbol{\omega}}|$. For example, for $|\tilde{\boldsymbol{\omega}}|/\sigma_{|\tilde{\boldsymbol{\omega}}|} \geqslant 4$, $1.5 \leqslant |\tilde{\boldsymbol{\omega}}|/\sigma_{|\tilde{\boldsymbol{\omega}}|} < 4$, and $|\tilde{\boldsymbol{\omega}}|/ < 1.5$, the peak values are 11.5, 3.7 and 1.3, respectively.

6. Discussion

After presenting a summary of the results in § 6.1, in § 6.2 we discuss the extent to which the results can be considered general characteristics of turbulent flows. The direct relationship between SGS dissipation and the strain–stress alignment is discussed in § 6.3. In § 6.4, some of the observed alignments are explained using dynamical and kinematical arguments. Finally, in § 6.5, we discuss the implications of the similarity between the $\tau_{ij}^d - \tilde{S}_{ij}$ and $\tau_{ij}^{nl} - \tilde{S}_{ij}$ alignment trends, and provide a motivation for development of improved SGS models. An Appendix provides additional results concerning the p.d.f. and conditional p.d.f.s of real and modelled SGS dissipation in order to demonstrate weaknesses and strengths in present SGS stress models.

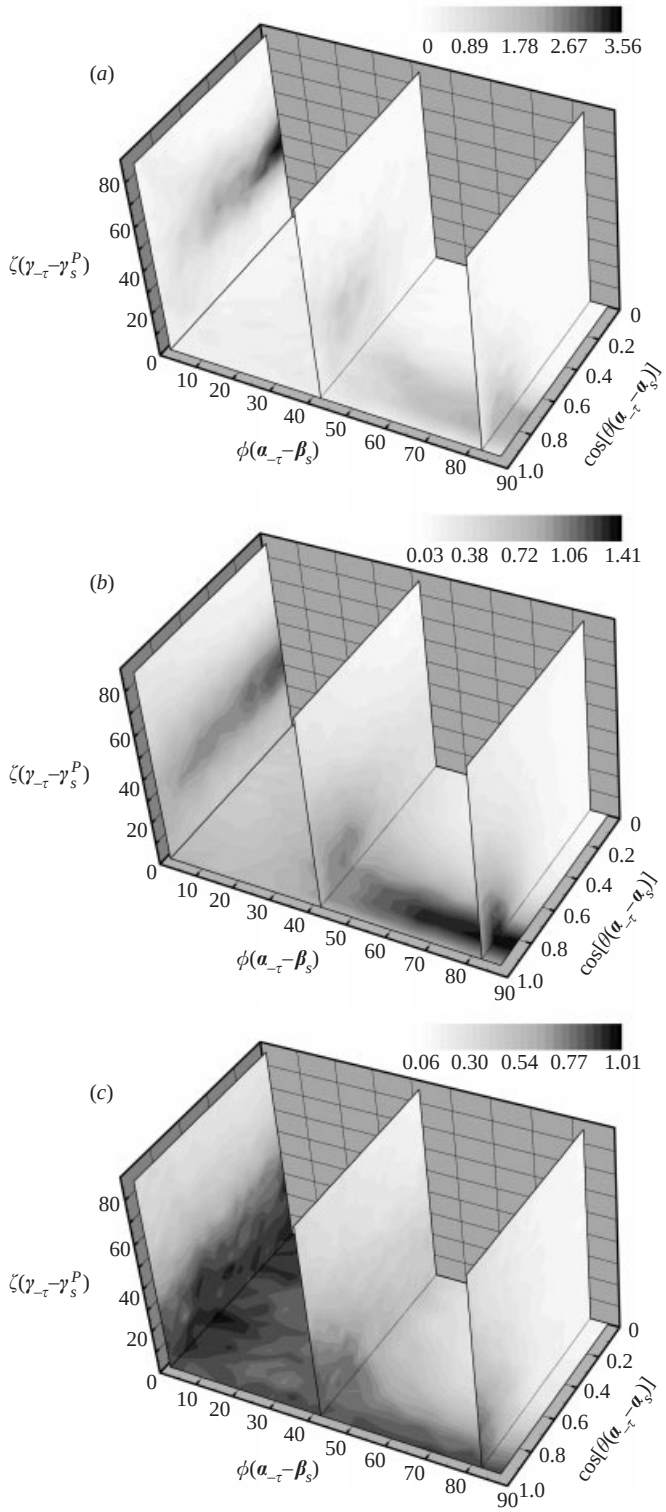

FIGURE 23. Conditional p.d.f.s of alignment between eigenvectors of $\tilde{S}_{ij}$ and $-\tau_{ij}^d$, based on the vorticity magnitude: (*a*) $|\tilde{\omega}|/\sigma_{|\tilde{\omega}|} \geqslant 4$, (*b*) $1.5 \leqslant |\tilde{\omega}|/\sigma_{|\tilde{\omega}|} < 4$, (*c*) $|\tilde{\omega}|/\sigma_{|\tilde{\omega}|} < 1.5$.

6.1. *Summary of results*

Briefly, the main findings of this paper are:

(i) The most extensive SGS stress eigenvector is preferentially aligned at 32° to the most contracting strain-rate eigenvector. This angle increases slightly (almost to 38°) with increasing magnitudes of filtered strain-rate and vorticity. In regions of low $|\tilde{\boldsymbol{S}}|$ and $|\tilde{\boldsymbol{\omega}}|$ the angle decreases to 0°, the p.d.f. peaks become very broad and decrease in magnitude.

(ii) The most contracting SGS stress eigenvector has a bimodal behaviour identified as configurations $\alpha\beta\gamma$–$\alpha\beta\gamma$ ($\boldsymbol{\alpha}_{-\tau}$ is at 32° to $\boldsymbol{\alpha}_s$) and $\alpha\beta\gamma$–$\beta\alpha\gamma$ ($\boldsymbol{\beta}_{-\tau}$ is at 32° to $\boldsymbol{\alpha}_s$). $\boldsymbol{\alpha}_{-\tau}$ is preferentially aligned with $\tilde{\omega}_i$ and parallel to $\boldsymbol{\beta}_s$ ($\alpha\beta\gamma$–$\beta\alpha\gamma$ configuration) in regions of high $|\tilde{\boldsymbol{\omega}}|$. This preference becomes stronger when $\beta_s > 0$. Since $\tilde{\omega}_i$ is also preferentially aligned with $\boldsymbol{\beta}_s$ (especially when $\beta_s > 0$) and with $\boldsymbol{\alpha}_{-\tau}$, these trends indicate when the vorticity is stretched by the intermediate strain-rate, the most contracting stress is preferentially aligned to oppose the motion that causes vortex stretching. In almost all the conditional samplings, both the most extensive and most contracting stress eigenvectors are not aligned with their corresponding eigenvectors of the filtered strain-rate, in contradiction to the fundamental assumption of eddy viscosity based models.

(iii) The measured stress eigenvectors are preferentially aligned at the same direction as those of the nonlinear (similarity) model. This orientation does not change with the magnitudes of strain, vorticity, s_τ^* and s^*. However, the p.d.f. peaks become lower and wider in regions of low $|\tilde{\boldsymbol{S}}|$, low $|\tilde{\boldsymbol{\omega}}|$, $s_\tau^* > 0$ and $s^* < 0$. This lack of sensitivity to varying conditions is an advantage of the nonlinear model over eddy viscosity based models. Stresses computed using the nonlinear model also have a bimodal behaviour, but the preferred angles are 42° instead of the measured 32°.

(iv) In agreement with the DNS results of Lund & Rogers (1994), the most probable strain state is axisymmetric extension ($s^* = 1$). In addition, the most probable SGS stress state corresponds to axisymmetric contraction ($s_\tau^* = -1$), and the probability of $s_\tau^* = -1$ is significantly higher than the probability of $s^* = 1$. The nonlinear model overestimates the probability of the preferred stress state. Joint p.d.f.s of s_τ^* and s^* show that the strain and stress states are mostly decoupled. The likelihood of high positive dissipation increases in regions of axisymmetric extension and in regions of axisymmetric contracting SGS stress. On the other hand, high negative SGS dissipation occurs more frequently in regions of axisymmetric contracting SGS stress, but remains independent of the strain-rate topology. Analysis of relationships between the nonlinear model dissipation and the strain-rate and stress topologies shows significant differences compared to the real dissipation especially in regions with negative s^* (towards axisymmetric contracting velocity field).

6.2. *Impact of inhomogeneity and mean flow conditions*

It is important to point out that trends discussed in this paper may be facility, flow or Reynolds-number dependent. However, as we have already demonstrated, the dominant phenomena, such as the stress–strain alignments and the relationships between s_τ^* and s_τ^{*nl}, are also observed in analysis using DNS data of isotropic turbulence (at lower *Re*). Another important issue concerns spatial inhomogeneity. In our analysis, we have averaged over the entire data set, i.e. over the entire wake region. To test for inhomogeneity, the data are divided into three parts: the 'inner section' is roughly the central $15 \times 15\,\mathrm{mm}^2$, the 'midsection' consists of a ~ 15 mm wide band that surrounds the inner section, and the 'outer section' is the outer ~ 15 mm wide band that surrounds the midsection. Based on measured velocity (mean and r.m.s. values

of fluctuations) presented, for example, in Melling & Whitelaw (1976), Eggeles *et al.* (1994) and Zhang *et al.* (1997), and consistent with our present data, the inner section has almost a uniform axial flow and almost 'isotropic' r.m.s. velocity fluctuations (see spectra in figure 4). The mean shear and anisotropy increase in the mid and outer sections. We have recomputed the joint p.d.f.s of figure 13 for each section separately. The results (not shown) demonstrate that the preferred alignments are essentially the same for the three sections, in spite of difference in the mean and fluctuating flow characteristics. The effects of filter size and type are other important questions. Based on previous results (Liu *et al.* 1994) we speculate that results for the Gaussian filter would be quite similar to present results for the box filter. However, owing to the spatially non-compact extent of the Gaussian and (especially) the spectral cutoff filters which interfere with the dataset's boundaries, we have not performed analyses using these filters. Limited analyses using larger filter sizes (e.g. 2Δ) did not show any important differences from results presented in this paper. These trends are strong indications that present results are not unique to our specific flow conditions and filter parameters. Nevertheless, to address fully the question of universality, the measurements and analysis should be repeated in several fundamentally different flow conditions, especially flows with high mean shear or rapidly strained turbulence. For the latter, for example, two-dimensional PIV data (Liu *et al.* 1999) shows that rapid straining causes substantial changes to the relationships between stresses and velocity gradients.

6.3. *Relationships between stress–strain alignments and SGS dissipation*

By its definition, $\Pi = -\tau_{ij}^d \tilde{S}_{ij}$, the SGS dissipation is strongly affected by how well each of the eigenvectors of τ_{ij}^d are aligned with those of $\tilde{S}_{ij}$. In order to identify which of the eigenvector alignments has the strongest effect in determining Π, we analyse the data and determine the SGS dissipation conditioned on the angles between respective eigenvectors. Distributions of the measured dissipation as a function of $\cos[\theta(\boldsymbol{\gamma}_{-\tau} - \boldsymbol{\gamma}_s)]$, $\cos[\theta(\boldsymbol{\beta}_{-\tau} - \boldsymbol{\beta}_s)]$ and $\cos[\theta(\boldsymbol{\alpha}_{-\tau} - \boldsymbol{\alpha}_s)]$ are plotted in figure 24(*a*). Although the dissipation increases with decreasing angle for all three cases, in two of them, $\theta(\boldsymbol{\alpha}_{-\tau} - \boldsymbol{\alpha}_s)$ and $\theta(\boldsymbol{\beta}_{-\tau} - \boldsymbol{\beta}_s)$, Π remains positive and the changes are much smaller than those occurring as $\theta(\boldsymbol{\gamma}_{-\tau} - \boldsymbol{\gamma}_s)$ varies. The dissipation becomes negative when $\theta(\boldsymbol{\gamma}_{-\tau} - \boldsymbol{\gamma}_s) > 56^\circ$.

Next, we develop simple expressions that allow us to understand better the relationship between preferred $\tau_{ij}^d - \tilde{S}_{ij}$ alignment and Π. For the preferred alignment configuration $\alpha\beta\gamma$–$\alpha\beta\gamma$, we have

$$\Pi_{\alpha\beta\gamma-\alpha\beta\gamma} = -\boldsymbol{\tau} : \boldsymbol{S}|_{\alpha\beta\gamma-\alpha\beta\gamma} = (\alpha_{-\tau}\alpha_s + \gamma_{-\tau}\gamma_s)\cos^2\theta + (\alpha_{-\tau}\gamma_s + \gamma_{-\tau}\alpha_s)\sin^2\theta + \beta_{-\tau}\beta_s. \quad (6.1)$$

Using $\beta_{-\tau} = -(\gamma_{-\tau} + \alpha_{-\tau})$ and $\beta_s = -(\gamma_s + \alpha_s)$, we obtain

$$\Pi_{\alpha\beta\gamma-\alpha\beta\gamma} = (\alpha_{-\tau}\alpha_s + \gamma_{-\tau}\gamma_s)(1 + \cos^2\theta) + (\alpha_{-\tau}\gamma_s + \gamma_{-\tau}\alpha_s)(1 + \sin^2\theta). \quad (6.2)$$

For the most probable strain and stress states $\gamma_{-\tau} = -2\alpha_{-\tau}$, $\gamma_s = -2\alpha_s$, and as a result

$$\Pi_{\alpha\beta\gamma-\alpha\beta\gamma}/(\alpha_{-\tau}\alpha_s) = \tfrac{3}{2}(1 + 3\cos 2\theta). \quad (6.3)$$

This expression becomes negative at $\theta > \cos(-\frac{1}{3})/2 \approx 55^\circ$, very close to the observed crossover value for $\theta(\boldsymbol{\gamma}_{-\tau} - \boldsymbol{\gamma}_s)$. These results indicate that the angle between the most contracting stress and most extensive strain has a dominant effect on the magnitude of dissipation.

In order to verify this statement, figure 24(*b*) shows the contribution of individual

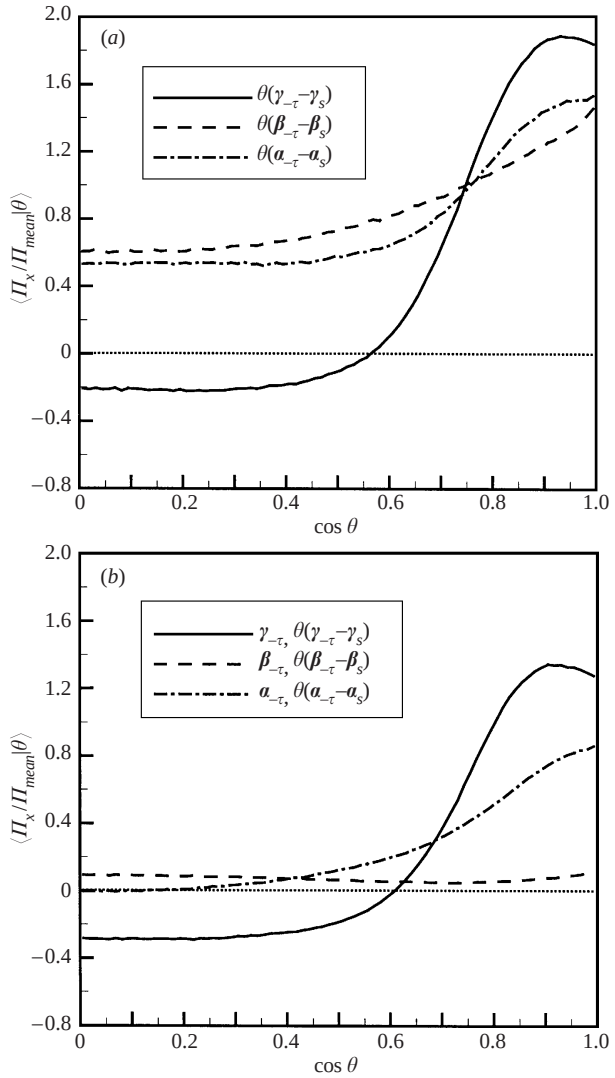

FIGURE 24. Mean SGS dissipation conditioned on the alignment angles between the eigenvectors of $\tilde{S}_{ij}$ and $-\tau^d_{ij}$: (*a*) overall dissipation rate, Π, (*b*) individual contributions to Π by the three eigenvectors of $-\tau^d_{ij}$.

stress components to the total dissipation. For example, the contribution of $\boldsymbol{\gamma}_{-\tau}$ is

$$\Pi_{\gamma_{-\tau}} = \gamma_{-\tau}\gamma_s \cos^2[\theta(\boldsymbol{\gamma}_{-\tau} - \boldsymbol{\gamma}_s)] + \gamma_{-\tau}\beta_s \cos^2[\theta(\boldsymbol{\gamma}_{-\tau} - \boldsymbol{\beta}_s)] + \gamma_{-\tau}\alpha_s \cos^2[\theta(\boldsymbol{\gamma}_{-\tau} - \boldsymbol{\alpha}_s)]. \quad (6.4)$$

The results show a slight shift in the angle of transition between positive and negative dissipation, from 56° to 61°, in the $\Pi_{\gamma-\tau}$ distribution conditioned on $\theta(\gamma_{-\tau} - \gamma_s)$. A comparison between figures 24(*a*) and 24(*b*) shows that although $\boldsymbol{\gamma}_{-\tau}$ is the dominant contributor to the overall dissipation, the contribution of the other two eigenvectors is not negligible. Unlike the distribution of Π as a function of $\theta(\boldsymbol{\alpha}_{-\tau} - \boldsymbol{\alpha}_s)$, $\Pi_{\alpha_{-\tau}}$ becomes slightly negative but very close to zero at large $\theta(\boldsymbol{\alpha}_{-\tau} - \boldsymbol{\alpha}_s)$. The distribution of $\Pi_{\beta_{-\tau}}$ is flat with very low positive values.

There are two reasons for the dominance of the terms involving $\boldsymbol{\gamma}_{-\tau}$. First, as the

p.d.f.s in figure 5 and the distributions of s^*_τ and s^* (figure 6) show, $\gamma_{-\tau}$ and γ_s are larger than the other eigenvalues. Secondly, as the alignment p.d.f.s demonstrate, the preferred orientation of $\boldsymbol{\gamma}_{-\tau}$ relative to $\tilde{S}_{ij}$ eigenvectors is consistent, does not have a bimodal behaviour and is less sensitive to varying parameters. Note also that the alignment of $\boldsymbol{\gamma}_{-\tau}$ can be estimated quite well using the nonlinear model (cf. figure 15), i.e. it is known during simulations. Consequently, figure 24 provides a tool to estimate the conditions under which the turbulence is prone to generation of negative dissipation.

6.4. *Dynamical and kinematical mechanisms underlying observed geometrical orientations*

The data show a consistent relative alignment between $\boldsymbol{\gamma}_{-\tau}$ and $\boldsymbol{\gamma}_s$, and a bimodal behaviour of the alignment between the other two eigenvectors. The $\alpha\beta\gamma$–$\beta\alpha\gamma$ configuration is much more pronounced in regions of high vorticity and the $\alpha\beta\gamma$–$\alpha\beta\gamma$ configuration becomes equally (or more) dominant in regions with intermediate levels of vorticity. We also find that some of these trends appear to be almost deterministic for the $\tau^{nl}_{ij} - \tilde{S}_{ij}$ alignment (figure 16).

In this section, we discuss possible dynamical and kinematical mechanisms that may help understand these observations. A plausible dynamical origin of the preferred $\alpha\beta\gamma$–$\beta\alpha\gamma$ alignment at high vorticity is the following: as a large-scale vortex filament oriented in the $\boldsymbol{\beta}_s$ direction (the most likely alignment of vorticity) is stretched, it becomes thinner and the velocity in directions perpendicular to the vortex axis increases. Owing to the decrease in size, some of this increased motion is transferred into the subgrid-scale range. This process increases the SGS stress normal components in the $(\boldsymbol{\alpha}_s, \boldsymbol{\gamma}_s)$-plane, but has little effect in the $\boldsymbol{\beta}_s$ direction. Since the eigenvectors are evaluated for the deviatoric part of the stress, an increase in the magnitude of only two components reduces the deviatoric part of the third component, i.e. the normal stress component in the $\boldsymbol{\beta}_s$ direction decreases. Thus, stretching of a large-scale vortex decreases the SGS stress element that is aligned with this vortex. When this vortex is powerful, this stress component is more likely to become the smallest (most contracting) stress. Consequently, the $\boldsymbol{\alpha}_{-\tau}$ eigenvector is more likely to be aligned with $\tilde{\omega}_i$ or $\boldsymbol{\beta}_s$ in regions of high $|\tilde{\boldsymbol{\omega}}|$.

Next, we discuss kinematical relationships that may explain some of the almost deterministic alignments between τ^{nl}_{ij} and $\tilde{S}_{ij}$ observed in § 4.2. The analysis is based on the measured preferred strain state and vorticity alignment. Expressing $\tilde{S}_{ij}$ and $\tilde{\omega}_i$ in the eigenframe of $\tilde{S}_{ij}$, we obtain:

$$\tilde{S}_{ij} = \alpha_s \boldsymbol{\alpha}_s \boldsymbol{\alpha}_s + \beta_s \boldsymbol{\beta}_s \boldsymbol{\beta}_s + \gamma_s \boldsymbol{\gamma}_s \boldsymbol{\gamma}_s, \tag{6.5}$$

$$\tilde{\omega}_i = \omega_\alpha \boldsymbol{\alpha}_s + \omega_\beta \boldsymbol{\beta}_s + \omega_\gamma \boldsymbol{\gamma}_s. \tag{6.6}$$

From the observations that $\tilde{\omega}_i$ is preferentially aligned with $\boldsymbol{\beta}_s$ (§ 5.4.1), and that the most probable strain state is axisymmetric extension (§ 3.1), we assume:

$$\omega_\alpha \approx \omega_\gamma \approx 0, \quad \omega_\beta \neq 0, \tag{6.7}$$

$$\alpha_s \approx \beta_s \approx -\tfrac{1}{2}\gamma_s. \tag{6.8}$$

Then, the filtered velocity gradient tensor becomes

$$\boldsymbol{A} = \nabla\tilde{\boldsymbol{u}} = \tilde{\boldsymbol{S}} + \tilde{\boldsymbol{\Omega}} = -\tfrac{1}{2}\gamma_s \begin{bmatrix} 1 & 0 & -r \\ 0 & 1 & 0 \\ r & 0 & -2 \end{bmatrix}, \tag{6.9}$$

where $r = \omega_\beta/\gamma_s$. The resulting deviatoric part of the nonlinear stress is

$$\tau_{ij}^{nl}/(C_{nl}\Delta^2) = A_{ki}A_{kj} - \tfrac{1}{3}\mathrm{tr}(A_{ki}A_{kj}) = \tfrac{1}{4}\gamma_s^2 T_{ij}, \tag{6.10}$$

where

$$\boldsymbol{T} = \begin{bmatrix} \frac{1}{3}r^2 - 1 & 0 & 3r \\ 0 & -(1+\frac{2}{3}r^2) & 0 \\ 3r & 0 & (2+\frac{1}{3}r^2) \end{bmatrix} \begin{matrix} \leftarrow \boldsymbol{\alpha}_s \\ \leftarrow \boldsymbol{\beta}_s \\ \leftarrow \boldsymbol{\gamma}_s \end{matrix}. \tag{6.11}$$

$\boldsymbol{T}$ can be diagonalized to

$$\boldsymbol{D} = \begin{bmatrix} \frac{1}{3}r^2 + \frac{1}{2}(1+3\sqrt{1+4r^2}) & 0 & 0 \\ 0 & -(1+\frac{2}{3}r^2) & 0 \\ 0 & 0 & \frac{1}{3}r^2 + \frac{1}{2}(1-3\sqrt{1+4r^2}) \end{bmatrix} \leftarrow \boldsymbol{\beta}_s. \tag{6.12}$$

Note that the transformation from T_{ij} to D_{ij} involves tensor rotation around the $\boldsymbol{\beta}_s$-axis. For $|r| < \sqrt{6}$, $\frac{1}{2} + \frac{1}{3}r^2 - \frac{3}{2}\sqrt{1+4r^2}$ is the most negative eigenvalue of T_{ij}, and thus the most positive eigenvalue of $-\tau_{ij}^{nl}$ is $\alpha_{-\tau}^{nl} = -C_{nl}\Delta^2\gamma_s^2(\frac{1}{2} + \frac{1}{3}r^2 - \frac{3}{2}\sqrt{1+4r^2})/4$. It follows that $\beta_{-\tau}^{nl} = C_{nl}\Delta^2\gamma_s^2(1+\frac{2}{3}r^2)/4$ remains the intermediate one. Considering that T_{ij} or τ_{ij}^{nl} is expressed in the eigenframe of $\tilde{S}_{ij}$, this alignment between eigenvectors of $-\tau_{ij}^{nl}$ and $\tilde{S}_{ij}$ resembles the $\alpha\beta\gamma$–$\alpha\beta\gamma$ configuration in figure 13(*a*). Conversely, for $|r| > \sqrt{6}$, $-(1+\frac{2}{3}r^2)$ becomes the most negative eigenvalue of T_{ij}, namely $\alpha_{-\tau}^{nl}$ and $\beta_{-\tau}^{nl}$ are switched. The resulting $\tau_{ij}^{nl} - \tilde{S}_{ij}$ alignment resembles the $\alpha\beta\gamma$–$\beta\alpha\gamma$ configuration.

In both cases, the angle between $\boldsymbol{\gamma}_{-\tau}^{nl}$ and $\boldsymbol{\gamma}_s$ or between $\boldsymbol{\alpha}_{-\tau}^{nl}$ and $\boldsymbol{\alpha}_s$ in the $(\boldsymbol{\alpha}_s, \boldsymbol{\gamma}_s)$-plane is:

$$\theta(\boldsymbol{\gamma}_{-\tau}^{nl} - \boldsymbol{\gamma}_s) = \cos^{-1}\left\{\left[2 + \frac{1}{2r^2}(1-\sqrt{1+4r^2})\right]^{-1/2}\right\}. \tag{6.13}$$

This angle varies depending on the parameter r. A first estimate of r can be given in terms of the r.m.s. values, i.e. $r \approx (\langle\omega_\beta^2\rangle/\langle\gamma_s^2\rangle)^{1/2}$. Using the isotropic turbulence relation $\langle\tilde{\omega}^2\rangle \approx 2\langle\tilde{s}_{ij}\tilde{s}_{ij}\rangle$ (Tennekes & Lumley 1972), and using $\langle\tilde{s}_{ij}\tilde{s}_{ij}\rangle = \langle\alpha_s^2 + \beta_s^2 + \gamma_s^2\rangle$ and (6.7) and (6.8), we obtain $r \approx \sqrt{3}$, and $\theta(\boldsymbol{\gamma}_{-\tau}^{nl} - \boldsymbol{\gamma}_s) \approx 36.9^\circ$ from (6.13). Note that since this result is for $|r| < \sqrt{6}$, this angle applies only to the $\alpha\beta\gamma$–$\alpha\beta\gamma$ alignment. If $r \approx (\langle\omega_\beta^2\rangle/\langle\gamma_s^2\rangle)^{1/2}$ is directly evaluated from the present data, we obtain $r \approx 1.81$ and $\theta(\boldsymbol{\gamma}_{-\tau}^{nl} - \boldsymbol{\gamma}_s) \approx 37.3^\circ$, i.e. in excellent agreement with the estimated value based on isotropy. For large values of r (high $|\tilde{\boldsymbol{\omega}}|$ and/or low $|\tilde{S}|$ regions), (6.13) shows that $\theta(\boldsymbol{\gamma}_{-\tau}^{nl} - \boldsymbol{\gamma}_s) \to 45^\circ$, not significantly different from the 42° alignment angle shown in figure 16.

6.5. *Implications and open issues*

The kinematic reasoning presented in the preceding section was successful in explaining several trends of the $\tau_{ij}^{nl} - \tilde{S}_{ij}$ alignment. In order to explore the implications on the alignment trends of the real SGS stress, we recall that the SGS stress can be decomposed into three distinct terms (Leonard 1974, but we use the Galilean invariant formulation of Germano 1986):

$$\tau_{ij}^{d} = \mathscr{L}_{ij} + \mathscr{C}_{ij} + \mathscr{R}_{ij}, \tag{6.14}$$

where $\mathscr{C}_{ij}$ is the so-called cross-stress, $\mathscr{R}_{ij}$ is the subgrid Reynolds stress, and $\mathscr{L}_{ij} = \widetilde{\tilde{u}_i\tilde{u}_j} - \tilde{\tilde{u}}_i\tilde{\tilde{u}}_j$ is the Galilean-invariant Leonard stress. Its Taylor series approximation is

$$L_{ij}^{*} = \tfrac{1}{12}\Delta^2 \frac{\partial\tilde{u}_i}{\partial x_k}\frac{\partial\tilde{u}_j}{\partial x_k}. \tag{6.15}$$

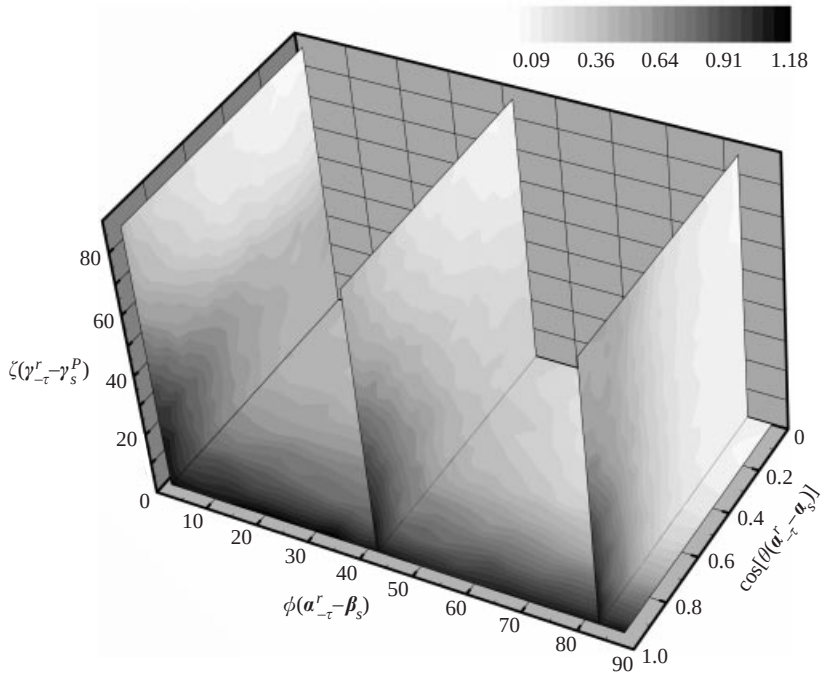

FIGURE 25. Joint p.d.f. of relative alignment between the residue stress, $-\psi^d_{ij}$, and $\tilde{S}_{ij}$. Here, $\boldsymbol{\alpha}^r_{-\tau}$ and $\boldsymbol{\gamma}^r_{-\tau}$ are the most contracting and most extensive eigenvectors of ψ^d_{ij}, respectively.

Equation (6.15) has the same form as the nonlinear model (1.6) except for the prefactor. Recognizing the apparent similarity between the $\tau^d_{ij} - \tilde{S}_{ij}$ and $\tau^{nl}_{ij} - \tilde{S}_{ij}$ alignments (figure 13*a vs.* figure 16), we may suspect that some of the non-trivial alignment trends (e.g. the bimodal behaviour) of the stress is due to the contribution of the resolved scales through the Leonard stress. To examine the impact of L^*_{ij} on the alignment trends we can subtract L^*_{ij} from τ^d_{ij} and observe the alignment of the residue stress, $\psi^d_{ij} = \tau^d_{ij} - L^{*d}_{ij}$, relative to $\tilde{S}_{ij}$. In the present analysis, L^*_{ij} is approximated by the filtered velocity gradients using the coarse grid, whereas the expression leading to (6.15) assumes that derivatives can be evaluated on a fine grid. Tests using the data show that setting the coefficient equal to 0.125 instead of $\frac{1}{12}$ in (6.15) minimizes the mean square error between $\mathscr{L}_{ij}$ and L^*_{ij}. Note that this coefficient is significantly smaller than the value of about $\frac{1}{3}$ for the nonlinear model which was quoted in Meneveau & Katz (1999*a*).

Indeed, as illustrated in figure 25, ψ^d_{ij} does not have the bimodal behaviour, and the preferred alignment shifts to $\theta(\boldsymbol{\alpha}^r_{-\tau} - \boldsymbol{\alpha}_s) \approx 0^\circ$ and $\zeta(\boldsymbol{\gamma}^r_{-\tau} - \boldsymbol{\gamma}^P_s) < 20^\circ$, i.e. a trend consistent with an eddy viscosity model for the remainder. Hence, we can conclude that a mixed model which adds L^{*d}_{ij} to the eddy viscosity term is supported by our results on alignment trends when considering non-conditioned p.d.f.s. Preliminary, more detailed, analysis that is to be described in a future publication reveals that problems still remain with such a mixed model formulation. For instance, conditional sampling shows that the bimodal peaks reappear in regions of high $|\tilde{\boldsymbol{S}}|$, high $|\tilde{\boldsymbol{\omega}}|$, and high Π. Furthermore, the 0.125 coefficient used here does not reproduce the magnitude of the stresses, whereas the earlier value close to $\frac{1}{3}$ did much better in that respect. Moreover, as shown in the Appendix, with this modified coefficient for

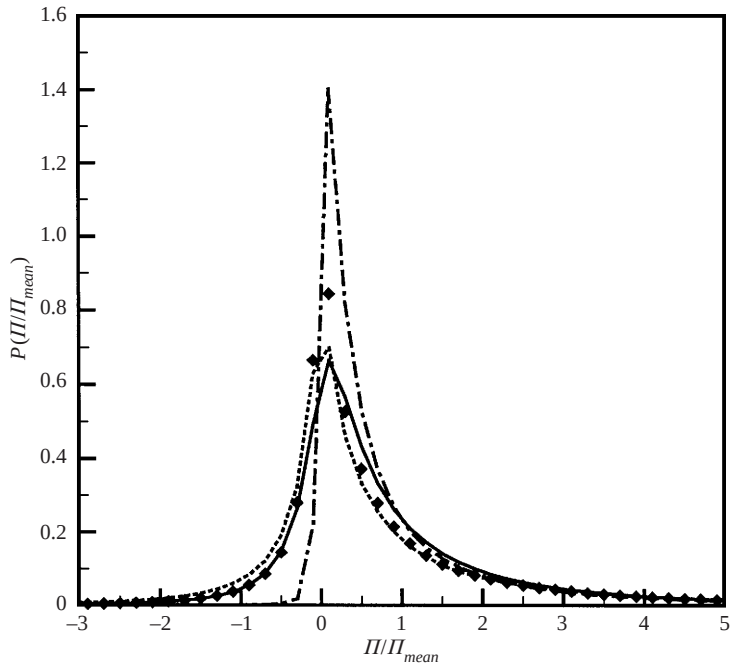

FIGURE 26. Probability density function of the SGS dissipation rate, evaluated from the experimental data, and by nonlinear and mixed models. ——, real dissipation; ···, nonlinear, $C_{nl} = 0.42$; ◆, mixed, $C_{nl} = 0.33$, $C_s = 0.09$; —·—; mixed, $C_{nl} = 0.125$, $C_s = 0.16$.

the nonlinear model part, the distribution of Π shows important differences from the real p.d.f.s, and also with conditional p.d.f.s in selected parts of the flow (e.g. high $|\tilde{\boldsymbol{S}}|$, high $|\tilde{\omega}|$, etc.). These results, along with the fact that the preferred alignment angles of the nonlinear and real stress with $\tilde{S}_{ij}$ are different (32° versus 42°), imply that simple subtraction of L_{ij}^* does not fully account for the bimodal alignment behaviour or SGS dissipation trends. Finally, we point out that even if the alignments were reproduced exactly by a model (which is unlikely), different eigenvectors might require different coefficients of proportionality. For instance, the differences in the s^* and s_τ^* p.d.f.s in § 3.1 indicate that such additional modifications may be required. These aspects should be investigated further.

We thank P. Dimotakis for an interesting discussion about three-dimensional alignments in turbulence. This work has been funded by the Office of Naval Research (grant N00014-98-1-0221, Drs P. Purtell and C. Wark, program managers), and in part by the National Science Foundation (L. Clark, program manager).

Appendix. Implications for SGS dissipation predicted by nonlinear and mixed models

In this Appendix we examine the distribution of SGS dissipation as predicted by the nonlinear and mixed models and comment on the effects of various flow parameters.

Figure 26 shows the comparison between the p.d.f. of the real SGS dissipation and those obtained from the nonlinear and mixed models. As is evident, the nonlinear model generates a larger number of points with high negative dissipation. The use of a mixed model (1.7) is to stabilize the nonlinear model by adding a dissipative

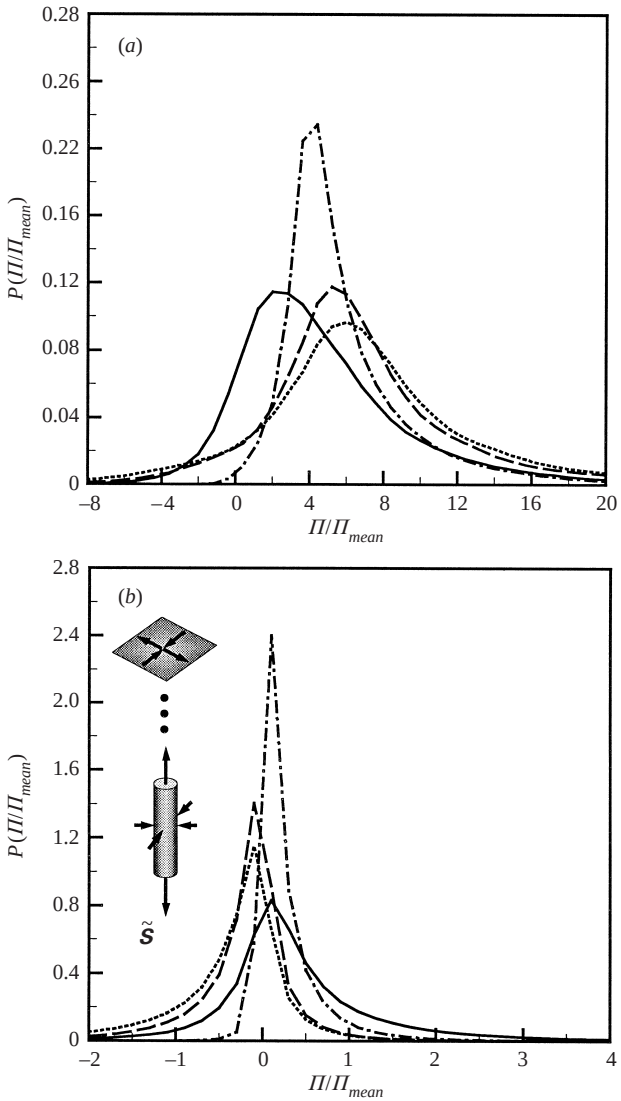

FIGURE 27. Conditional p.d.f.s of the SGS dissipation rate: (*a*) $|\tilde{S}|/\sigma_{|\tilde{S}|} \geqslant 4$, and (*b*) $s^* < 0$. ——, real dissipation; · · ·, nonlinear; – –, mixed, $C_{nl} = 0.33$, $C_s = 0.09$; — · —, mixed, $C_{nl} = 0.125$, $C_s = 0.16$.

Smagorinsky term. For the mixed model, we show results for two values of C_{nl}. The first is $C_{nl} = 0.33$ for the nonlinear model and $C_s = 0.09$ for the Smagorinsky term. These values are very similar to those suggested in Meneveau & Katz (1999*b*), which reproduce the mean dissipation correctly, and also the predicted stress magnitudes are close to those of the real SGS stress. The second choice is $C_{nl} = 0.125$ and $C_s = 0.16$. These values are motivated by our results on alignments of the residue stress ψ_{ij}^d, and C_s is adjusted to produce the correct Π_{mean}. Figure 26 shows that the p.d.f. of the mixed model for the $C_{nl} = 0.33$ case improves the prediction in the backscatter range, whereas the $C_{nl} = 0.125$ case is too dissipative, which predicts significantly fewer occurrences of backscatter. This behaviour also exists in various conditional dissipation p.d.f.s.

The agreement between the mixed model ($C_{nl} = 0.33$) and real SGS dissipation is

not uniformly valid in all regions of the flow. For example, conditional sampling based on strain-rate magnitude, as illustrated in figure 27(*a*), shows that in regions with high strain-rate, all three models predict excessive occurrences of positive dissipation. Conditional sampling based on s^* also leads to substantial discrepancies, especially in regions when $s^* < 0$ (figure 27*b*). Here, both the nonlinear model and the mixed model ($C_{nl} = 0.33$) are strongly skewed toward the negative side, consistent with the differences between the joint p.d.f.s shown in figures 9(*a*) and 9(*c*). Considering that $s^* < 0$ occurs in 32.4% of the sample volume, the results in figure 27(*b*) should raise serious concerns. Similar discrepancies occur as a result of conditional samplings based on other parameters.

In summary, taking all the data as a whole, the dissipation p.d.f. of the mixed model (with $C_{nl} = 0.33$) seems to agree with that of the real dissipation. However, in regions with high $|\tilde{\boldsymbol{S}}|$, it is too dissipative, whereas in regions with negative s^*, it still produces significantly more negative dissipation. Knowledge of where the corrections are needed may guide the development of improved models.

REFERENCES

Adrian, R. J. 1990 Stochastic estimation of subgrid scale motions. *Appl. Mech. Rev.* **43**, S214.

Ashurst, W. T., Kerstein, A. R., Kerr, R. M. & Gibson, C. H. 1987 Alignment of vorticity and scalar gradient with strain rate in simulated Navier–Stokes turbulence. *Phys. Fluids* **30**, 2343.

Bardina, J., Ferziger, J. H. & Reynolds, W. C. 1980 Improved subgrid scale models for large-eddy simulation. *AIAA Paper* 80–1357.

Bastiaans, R., Rindt, C. & van Steenhoven, A. 1998 Experimental analysis of a confined transitional plume with respect to subgrid-scale modeling. *Intl J. Heat Mass Transfer* **41**, 3989.

Borue, V. & Orszag, S. 1998 Local energy flux and subgrid-scale statistics in three-dimensional turbulence. *J. Fluid Mech.* **366**, 1.

Cantwell, B. J. 1992 Exact solution of a restricted Euler equation for the velocity gradient tensor. *Phys. Fluids* A **4**, 782.

Cerutti, S. & Meneveau, C. 1998 Intermittency and relative scaling of subgrid-scale energy dissipation in isotropic turbulence. *Phys. Fluids* **10**, 928.

Cerutti, S., Meneveau, C. & Knio, O. M. 2000 Spectral and hyper eddy viscosity in high-Reynolds-number turbulence. *J. Fluid Mech.* **421**, 307.

Chertkov, M., Pumir, A. & Shraiman, B. I. 1999 Lagrangian tetrad dynamics and the phenomenology of turbulence. *Phys. Fluids* **11**, 2394.

Domaradski, J. A. & Saiki, E. M. 1997 A subgrid-scale model based on the estimation of unresolved scales of turbulence. *Phys. Fluids* **9**, 1.

Eggeles, J. G. M., Unger, F., Weiss M. H., Westerweel, J., Adrian, R. J., Friedrich, R. & Nieuwstad, F. T. M. 1994 Fully developed turbulent pipe flow: a comparison between direct numerical simulation and experiment. *J. Fluid Mech.* **268**, 175.

Germano, M. 1986 A proposal for a redefinition of the turbulent stresses in the filtered Navier–Stokes equations. *Phys. Fluids* **29**, 2323.

Langford, J. & Moser, R. 1999 Optimal LES formulations for isotropic turbulence. *J. Fluid Mech.* **398**, 321.

Leonard, A. 1974 Energy cascade in large-eddy simulations of turbulent fluid flows. *Adv. Geophys.* **18**, 237.

Lesieur, M. & Métais, O. 1996 New trends in large-eddy simulations of turbulence. *Annu. Rev. Fluid Mech.* **28**, 45.

Liu, S., Katz, J. & Meneveau, C. 1999 Evolution and modelling of subgrid scales during rapid straining of turbulence. *J. Fluid Mech.* **387**, 281.

Liu, S., Meneveau, C. & Katz, J. 1994 On the properties of similarity subgrid-scale models as deduced from measurements in a turbulent jet. *J. Fluid Mech.* **275**, 83.

Liu, S., Meneveau, C. & Katz, J. 1995 Experimenal study of similarity subgrid-scale models of turbulence in the far-field of a jet. *Appl. Sci. Res.* **54**, 17.

Lund, T. & Rogers, M. 1994 An improved measure of strain state probability in turbulent flows. *Phys. Fluids* **6**, 1838.

McComb, W. D. & Watt A. G. 1990 Conditional averaging procedure for the elimination of the small-scale modes from incompressible fluid turbulence at high Reynolds numbers. *Phys. Rev. Lett*. **65**, 3281.

Melling, A. & Whitelaw, J. H. 1976 Turbulent flow in a rectangular duct. *J. Fluid Mech.* **78**, 289.

Meneveau, C. & Katz, J. 1999*a* Conditional subgrid force and dissipation in locally isotropic and rapidly strained turbulence. *Phys. Fluids* **11**, 2317.

Meneveau, C. & Katz, J. 1999*b* Dynamic testing of subgrid models in large eddy simulation based on the Germano identity. *Phys. Fluids* **11**, 245.

Meneveau, C. & Katz, J. 2000 Scale-invariance and turbulence models for large-eddy simulation. *Annu. Rev. Fluid Mech.* **32**, 1.

Misra, A. & Pullin, D. I. 1997 A vortex-based subgrid stress model for large-eddy simulation. *Phys. Fluids* **9**, 2443.

Moin, P. & Mahesh, K. 1998 Direct numerical simulation: a tool in turbulence research. *Annu. Rev. Fluid Mech.* **30**, 539.

O'neil, J. & Meneveau, C. 1997 Subgrid-scale stresses and their modelling in the turbulent plane wake. *J. Fluid Mech.* **349**, 253.

Piomelli, U. 1999 Large-eddy simulation: achievements and challenges. *Prog. Aerospace Sci.* **35**, 335.

Piomelli, U., Cabot, W. H., Moin, P. & Lee, S. 1991 Subgrid-scale backscatter in turbulent and transitional flows. *Phys. Fluids* A **3**, 1766.

Piomelli, U., Moin, P. & Ferziger, J. H. 1988 Model consistency in large eddy simulation of turbulent channel flows. *Phys. Fluids* **31**, 1884.

Porté-agel, F., Parlange, M. B., Meneveau, C. & Eichinger, W. E. 2000 A-priori field study of the subgrid-scale heat fluxes and dissipation in the atmospheric surface layer. *J. Atmos. Sci.* Submitted.

Roth, G. I., Hart, D. & Katz, J. 1995 Feasibility of using the L64720 video motion estimation processor (MEP) to increase efficiency of velocity map generation for PIV. *Proc. ASME/EALA 6th Intl Symp. on Laser Anemometry*, FED **229**, 387.

Roth, G. I. & Katz, J. 2001 Five techniques for increasing the speed and accuracy of PIV interrogation. *Meas. Sci. Technol.* **12**, 238.

Schlichting, H. 1979 *Boundary-layer Theory*, 7th edn. McGraw-Hill.

Scotti, A. & Meneveau, C. 1999 A fractal model for large eddy simulation of turbulent flow. *Physica* D **127**, 198.

Tao, B. 2000 Development of holographic particle image velocimetry and its application in three-dimensional velocity measurement and modeling of high Reynolds number turbulent flows. PhD thesis, The Johns Hopkins University, Baltimore, MD.

Tao, B., Katz, J. & Meneveau C. 1999*a* Applications of HPIV data of turbulent duct flow for turbulence modeling. *Proc. ASME Summer Meeting Paper FEDSM99-7281.*

Tao, B., Katz, J. & Meneveau C. 2000 Geometry and scale relationships in high Reynolds number turbulence determined from three-dimensional holographic velocimetry. *Phys. Fluids* **12**, 941.

Tao, B., Malkiel, E. & Katz, J. 1999*b* Analysis tools for holographic particle image velocimetry (HPIV). Presented at *3rd Intl Workshop on Particle Image Velocimetry, 16–18, September 1999, Santa Barbara, CA.*

Tennekes, H. & Lumley, J. L. 1972 *A First Course in Turbulence*. The MIT Press.

Tsinober, A., Kit, E. & Dracos, T. 1992 Experimental investigation of the field of velocity gradients in turbulent flows. *J. Fluid Mech.* **242**, 169.

Vincent, A. & Meneguzzi, M. 1994 The dynamics of vorticity tubes in homogeneous turbulence. J. Fluid Mech. **258**, 245.

Zhang, J., Tao, B. & Katz, J. 1997 Turbulent flow measurement in a square duct with hybrid holographic PIV. *Exps. Fluids* **23**, 373.